Spectroscopic Evidence for Ca^{2+} Involvement in the Assembly of the Mn_4Ca Cluster in the Photosynthetic Water-Oxidizing Complex[†]

Alexei M. Tyryshkin,[*,‡] Richard K. Watt,[§] Sergei V. Baranov,[||] Jyotishman Dasgupta, Michael P. Hendrich,[⊥] and G. Charles Dismukes[*]

Department of Chemistry and the Princeton Environmental Institute, Princeton University, Princeton, New Jersey 08544, and Department of Chemistry, Carnegie Mellon University, Pittsburgh, Pennsylvania 15213

Received July 25, 2006; Revised Manuscript Received August 18, 2006

ABSTRACT: Biogenesis and repair of the inorganic core ($Mn_4CaO_xCl_y$), in the water-oxidizing complex of photosystem II (WOC−PSII), occurs through the light-induced (re)assembly of its free elementary ions and the apo-WOC−PSII protein, a reaction known as photoactivation. Herein, we use electron paramagnetic resonance (EPR) spectroscopy to characterize changes in the ligand coordination environment of the first photoactivation intermediate, the photo-oxidized Mn^{3+} bound to apo-WOC−PSII. On the basis of the observed changes in electron Zeeman (g_{eff}), ^{55}Mn hyperfine (A_Z) interaction, and the EPR transition probabilities, the photogenerated Mn^{3+} is shown to exist in two pH-dependent forms, differing in terms of strength and symmetry of their ligand fields. The transition from an EPR-invisible low-pH form to an EPR-active high-pH form occurs by deprotonation of an ionizable ligand bound to Mn^{3+}, implicated to be a water molecule: $[Mn^{3+}(OH_2)] \leftrightarrow [Mn^{3+}(OH^-)]$. In the absence of Ca^{2+}, the EPR-active Mn^{3+} exhibits a strong pH dependence (pH ∼6.5−9) of its ligand-field symmetry (rhombicity $\Delta\delta = 10\%$, derived from g_{eff}) and A_Z ($\Delta A_Z = 22\%$), attributable to a protein conformational change. Binding of Ca^{2+} to its effector site eliminates this pH dependence and locks both g_{eff} and A_Z at values observed in the absence of Ca^{2+} at alkaline pH. Thus, Ca^{2+} directly controls the coordination environment and binds close to the high-affinity Mn^{3+}, probably sharing a bridging ligand. This Ca^{2+} effect and the pH-induced changes are consistent with the ionization of the bridging water molecule, predicting that $[Mn^{3+}-(\mu\text{-}O^{-2})-Ca^{2+}]$ or $[Mn^{3+}-(\mu\text{-}OH^-)_2-Ca^{2+}]$ is the first light intermediate in the presence of Ca^{2+}. The formation of this intermediate templates the apo-WOC−PSII for the subsequent rapid cooperative binding and photo-oxidation of three additional Mn^{2+} ions, forming the active water oxidase.

A single tight-binding Ca^{2+} ion is essential for photosynthethic O_2 evolution activity *in vivo* (*1−5*). Calcium is located within the water-oxidizing complex of photosystem II (PSII−WOC),[1] comprised of an oxo/aquo-bridged inorganic core whose stoichiometry, Mn_4CaO_x, is based on several lines of evidence, including X-ray absorption (*6−9*), electron paramagnetic resonance (EPR) spectroscopy (*10, 11*), and the recent X-ray diffraction (XRD) data (*12, 13*). Mn-, Sr-, and Ca-extended X-ray absorption fine structure (EXAFS) spectroscopies accurately place the calcium effector

site at 3.3−3.5 Å from Mn atoms. However, the relative position of Ca^{2+} within the Mn_4O_x cluster differs according to which type of data is emphasized and the assumptions of the models used to interpret the raw data. Spectroscopic and XRD data have constrained the possible core topologies to only a few types, with the structures given in Chart 1 proposed on the basis of one or more lines of evidence (*9−11, 13*). These structural proposals have led to a number of mechanistic proposals for the role of calcium in O_2 evolution reviewed elsewhere (*11, 14−17*).

Dissection of the functional roles of the inorganic cofactors has come from *in vitro* studies of the photoactivation process, which is defined as the assembly of the inorganic core during biogenesis and repair of the WOC. *In vitro* photoactivation of the WOC is described by the following cofactor stoichiometry (for a review, see refs *18* and *19*):

$$[\text{apo-WOC−PSII}] + 4Mn^{2+} + 1Ca^{2+} + yCl^- \xrightarrow{h\nu,\ HCO_3^-} [Mn_4O_xCa_1Cl_y] + nH^+ \quad (1)$$
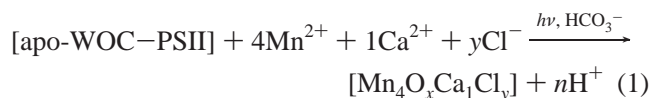
Photoactivation is a multistep process in which the inorganic core is assembled in a preferred sequence of light-induced photo-oxidation steps and dark steps. A minimal kinetic model, given by eq 2, lists the kinetic intermediates that have

* To whom correspondence should be addressed. Telephone: 609-258-4167. E-mail: atyryshk@princeton.edu (A.M.T.); Telephone: 609-258-3949. Fax: 609-258-1980. E-mail: dismukes@princeton.edu (G.C.D.).

‡ Present address: Department of Electrical Engineering, Princeton University, Princeton, NJ.

§ Present address: University of New Mexico, Albuquerque, NM.

|| Present address: Burke Medical Research Institute, White Plains, NY.
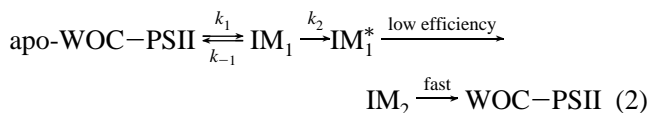
⊥ Present address: Carnegie Mellon University, Pittsburgh, PA.

1 Abbreviations: DCBQ, 2,5-dichloro-*p*-benzoquinone; CHES, 2-(cyclohexylamino)ethanesulfonic acid; EPR, electron paramagnetic resonance; HEPES, *N*-(2-hydroxyethyl)piperazine-*N'*-(2-ethanesulfonic acid); MES, 2-(*N*-morpholino)ethanesulfonic acid; PSII, photosystem II; WOC, water-oxidizing complex; ZFS, zero-field splitting.

Chart 1: Possible Structural Candidates for the Mn$_4$Ca Core of the WOC in PSII Based on Single-Crystal Mn EXAFS (Structures 1−3) or XRD (Structure 4) Studies (*9, 13*)
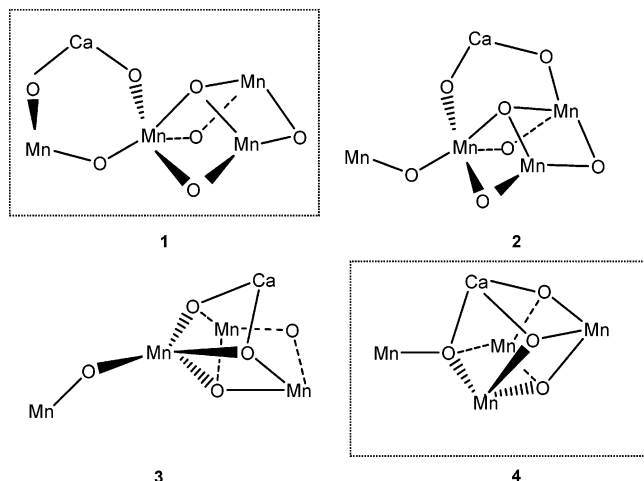
been resolved during *in vitro* photoactivation of spinach PSII membranes (*20−23*).

$$\text{apo-WOC−PSII} \underset{k_{-1}}{\overset{k_1}{\rightleftharpoons}} \text{IM}_1 \overset{k_2}{\rightarrow} \text{IM}_1^* \overset{\text{low efficiency}}{\longrightarrow}$$

$$\text{IM}_2 \overset{\text{fast}}{\longrightarrow} \text{WOC−PSII} \quad (2)$$

The first light-induced step is reversible (pseudo-first-order rate constants given by k_1 and k_{-1}) and involves binding and photo-oxidation of Mn^{2+} to Mn^{3+} to form the first assembly intermediate, IM$_1$ (*20, 23*). Bicarbonate ions play an important physiological role in accelerating the rate and increasing the yield of the first intermediate in photoactivation (*24−26*). The second step (k_2) is rate-limiting and occurs in the dark, and its overall slowness suggests that it involves a protein conformational change. Under low Ca^{2+} concentrations (<1 mM) when it is not bound to its effector site, this step is coupled to an increase in its binding affinity (*23*). Upon illumination, a second Mn^{2+} binds and oxidizes with low quantum efficiency to produce a long-lived intermediate, denoted IM$_2$, which contains two Mn^{3+} and Ca^{2+} (*19, 21, 22*). This state has never been directly observed because it can advance to the fully reassembled WOC by rapid uptake of the remaining two Mn^{2+} ions in a highly cooperative kinetically unresolved step that represents the most efficient pathway to an active cluster. If Ca^{2+} is not included during photoactivation, a large excess of Mn^{2+} is photo-oxidized and O$_2$ evolution is not restored (*27*). This inactivation process can be reversed by adding Ca^{2+}, which restores a normal Mn$_4$O$_x$ core, clearly establishing a role for calcium in guiding the assembly of the catalytically active Mn$_4$O$_x$ core and restructuring the inactive polymanganese-oxo cluster (*18, 28, 29*).

Other nonphysiological low-affinity Ca^{2+} site(s) further stimulate the O$_2$ activity of isolated PSII membranes and photoactivated apo-WOC−PSII membranes (*30, 31*) but are not required for inorganic core assembly, and the stimulation of O$_2$ evolution that they produce is reduced if peripheral extrinsic proteins removed during PSII isolation are restored. Although chloride ions are physiologically essential for the expression of O$_2$ evolution activity of PSII (*32*), they are not known to play any role in the assembly of the inorganic

cofactors during photoactivation and appear to be external to the core [(*33−35*) also reviewed in ref *36*].

Several studies have applied EPR spectroscopy to examine the kinetics and cofactors required for photoactivation, including the loss of the Mn^{2+} signal intensity upon photo-oxidation by apo-WOC−PSII (*37*), reduction of tyrosine Y$_Z^{\cdot}$ by Mn^{2+} (*38*), and activation of Mn^{2+} for electron donation by bicarbonate (*39*). Campbell et al. have reported the EPR spectrum of the initial photo-oxidized Mn^{3+} assembly intermediate in PSII core particles from *Synechocystis* and used this data to describe the symmetry of the ligand field (*40*). Herein, we extend this approach to examine the initial photo-oxidized Mn^{3+} intermediates formed as a function of pH and Ca^{2+} binding. We derive new expressions from the ligand-field theory and apply them to achieve a molecular interpretation of the experimental EPR parameters in terms of the ligand environment of Mn^{3+}.

MATERIALS AND METHODS

PSII-enriched membrane fragments were prepared from market spinach by the method described elsewhere (*41, 42*). Under saturating continuous illumination, the oxygen evolution rate of the PSII membranes was 400−500 μmol of O$_2$ (mg of Chl)$^{-1}$ h^{-1} in the presence of 1 mM K$_3$Fe(CN)$_6$ and 0.25 mM 2,5-dichloro-p-benzoquinone (DCBQ) as electron acceptors. PSII membranes depleted of Mn^{2+}, Ca^{2+}, and the three extrinsic proteins (apo-WOC−PSII) were prepared by a brief incubation in high-pH buffer in the presence of 200 mM MgCl$_2$, as recently described (*25*). The resulting apo-WOC−PSII membranes were devoid of the three extrinsic proteins as confirmed by SDS−PAGE (not shown) and exhibited no residual O$_2$ evolution activity (i.e., less than 0.5% of the activity of the BBY membranes). These apo-WOC−PSII particles were capable of reconstituting the water-splitting system of PSII (upon *in vitro* photoactivation in the presence of Mn^{2+}, Ca^{2+}, and an electron acceptor) with a yield of 60−70% as calibrated versus the extrinsic protein-depleted PSII (*25*).

For EPR spectroscopy, apo-WOC−PSII samples were suspended at 1 mg of Chl/mL in buffer containing 300 mM sucrose, 35 mM NaCl, and 30 mM 2-(N-morpholino)-ethanesulfonic acid (MES)/NaOH (pH 6). The samples were briefly illuminated (to photo-oxidize any reduced tyrosine-D or Y$_D$), dark-adapted for 5 min at 4 °C, centrifuged, and resuspended to 5 mg of Chl/mL (20 μM PSII) in either MES/NaOH (pH 6−6.5), N-(2-hydroxyethyl)piperazine-N'-(2-ethanesulfonic acid) (HEPES)/NaOH (pH 7.5), or 2-(cyclo-hexylamino)ethanesulfonic acid (CHES)/NaOH (pH 9.0). Then, the indicated amount of MnCl$_2$ and CaCl$_2$ was added to the samples in the dark, and after mixing and 15 min of additional incubation, the samples were moved to EPR tubes and frozen to 77 K. Precision quartz tubes were used to prepare identical sample volumes suitable for quantitative comparisons of the measured EPR signals. To photo-oxidize Mn^{2+}, the samples were illuminated at −20 °C by a 300 W halogen lamp filtered with a 3% solution of CuSO$_4$. Illumination at lower than −20 °C or higher temperatures produces a lower yield of photo-oxidized Mn^{3+} as described in the Results. EPR measurements were made in triplicate using a Bruker Elexsys 580 X-band spectrometer and Bruker ER 4116DM dual-mode EPR cavity. The EPR measurements
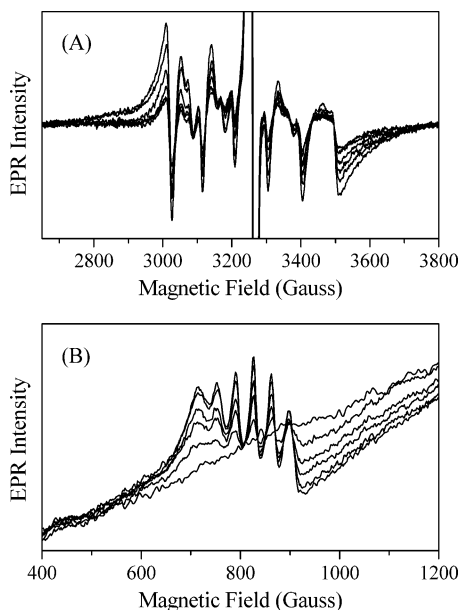
FIGURE 1: Mn^{2+} (top) and Mn^{3+} (bottom) EPR signals in apo-WOC−PSII (20 μM) in the presence of 120 μM Mn^{2+} (6 Mn^{2+}/PSII) after illumination at −20 °C for variable times (1, 3, 6, 11, and 18 min). The sample contains 10 mM Ca^{2+} (HEPES at pH 7.5). Perpendicular-mode EPR (Mn^{2+}) was performed at 77 K, and parallel-mode EPR (Mn^{3+}) was performed at 3.7 K. Other experimental conditions are described in the Materials and Methods.

of Mn^{2+} were performed using perpendicular-mode excitation at a temperature of 77 K (liquid N_2 finger dewar), at microwave frequency of 9.13 GHz, microwave power of 0.8 mW, and modulation amplitude of 0.5 mT. Mn^{3+} EPR was measured using parallel-mode excitation at 3.7 K with an Oxford ESR 900 helium flow cryostat, at microwave frequency of 9.175 GHz, microwave power of 50 mW, and modulation amplitude of 1 mT.

RESULTS

Illumination at −20 °C Produces a Maximal Yield of Mn^{3+}. Figure 1 illustrates the decay of the Mn^{2+} EPR signal (Figure 1A) and the parallel growth of the Mn^{3+} signal (Figure 1B) induced by illumination of apo-WOC−PSII at −20 °C. This light-induced Mn^{3+} originates from the photo-oxidation of Mn^{2+} bound to the donor side of PSII (*38, 40, 43*). The Mn^{3+} signal is stable in the dark at −20 °C (for over 15 min), indicating that dark processes, such as diffusion of Mn^{2+}/Ca^{2+} cofactors and protein conformational changes, are significantly slowed at this temperature. In particular, the diffusion of Mn^{2+} and Ca^{2+} is not permitted because, otherwise, it should cause a dark decay/change in the Mn^{3+} EPR signal through re-reduction/dissociation processes and/or spontaneous assembly of the next assembly intermediate upon binding a second Mn^{2+}. However, diffusion processes become more important when the temperature is raised to −10 °C and above, as is evidenced by the instability of the Mn^{3+} signal, which decays in the dark within a minute. Conversely, the equivalent illumination time at temperatures lower than −20 °C produces a smaller Mn^{3+} signal (i.e., 50% and 20−30% at −30 and −40 °C, respectively). This loss is due to the limitation of $Q_A \rightarrow Q_B$ electron transport on the acceptor side of PSII (*44*) and/or by proton ionization on the donor side. Accordingly, we used the optimal temperature −20 °C to produce the maximal yield of the
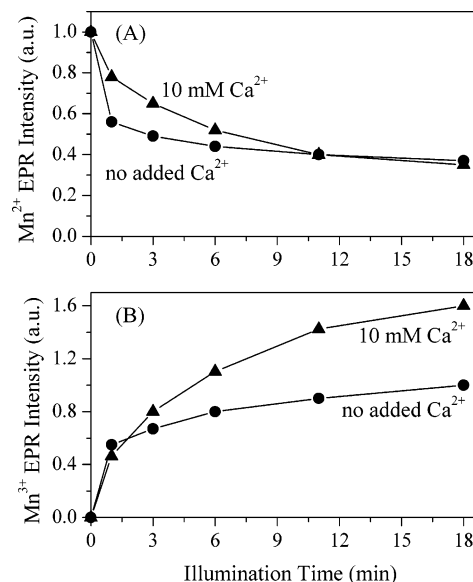

FIGURE 2: Light-induced decay of the Mn^{2+} (top) and growth of the Mn^{3+} (bottom) EPR signal intensities versus illumination time at −20 °C: (●) no added Ca^{2+} and (▲) 10 mM Ca^{2+}. The sample contains 20 μM apo-WOC−PSII and 120 μM Mn^{2+} (HEPES at pH 7.5). Other conditions are the same as in Figure 1. All EPR results were obtained in triplicate.

photo-oxidized Mn^{3+}. Because diffusion of Mn^{2+}/Ca^{2+} cofactors is frozen-out, this Mn^{3+} corresponds to the oxidation of the Mn^{2+} that is bound to the donor side of PSII in the dark, prior to freezing to −20 °C.

Upon illumination at −20 °C, only the Mn^{3+} signal was produced, and in the range of the Mn^{2+} concentration from 10 to 320 μM (0.5−16 Mn^{2+}/PSII), no EPR spectral evidence was found for signals arising from either double oxidation that forms Mn^{4+} or single turnovers that form spin-coupled mixed-valence dimers such as Mn^{3+}−Mn^{2+}. Both types of EPR signals are easily observable and differ spectrally from Mn^{2+} and Mn^{3+} based on extensive literature of model complexes (*45−47*). Thus, we conclude that no photo-oxidizable Mn^{2+}−Mn^{2+} dimer structures are preformed in the dark prior to freezing at −20 °C, neither in the absence or presence of 10 mM Ca^{2+}.

Inspection of Figure 1 reveals that only the signal intensities change, while the shape of both the Mn^{2+} and Mn^{3+} signals does not change with the illumination time. The signal intensities are plotted in Figure 2 for apo-WOC−PSII samples containing an excess of 6 Mn^{2+}/PSII and with 10 mM Ca^{2+} or no added Ca^{2+}. A close correlation is seen between the loss of the Mn^{2+} signal and the increase of the Mn^{3+} signal on illumination time, suggesting a direct conversion with no detectable intermediate (see overlaid traces for a direct comparison in Figure S3 in the Supporting Information). The rate of photoaccumulation of Mn^{3+} and photobleaching of Mn^{2+} is slower in the presence of 10 mM Ca^{2+} (or 10 mM Mg^{2+}, not shown), probably because of cation-induced PSII membrane aggregation, which results in an altered optical transparency of the samples. Alternatively, Ca^{2+} binding in close proximity to the photo-oxidizable Mn^{2+} may alter (reduce) the efficiency of Mn^{2+} oxidation, thus resulting in slower oxidation kinetics (reviewer's suggestion). Regardless of the presence of divalent cations (Ca^{2+} or Mg^{2+}), the loss of the Mn^{2+} signal saturates at the same level, indicating that approximately the same

amount of Mn^{2+} is photo-oxidized. A quantitative interpretation of the Mn^{2+} signal intensity in terms of the number and symmetry of the oxidized Mn^{2+} is complicated by the unknown speciation of Mn^{2+} in the PSII samples (i.e., both specific and nonspecific Mn^{2+} sites on PSII and free Mn^{2+} in solution) (*43*). This complexity results in a large number of unknowns, and thus, a quantitative analysis of the Mn^{2+} EPR line shape was not undertaken. However, qualitatively, we conclude that substantial and comparable fractions of Mn^{2+} are oxidized in both samples, i.e., with and without added Ca^{2+}.

We were unable to quantify the amount of Mn^{2+} taken up from solution by apo-WOC−PSII during illumination at −20 °C, using another well-established method that involves washing the sample with Mn-free buffer to remove free (e.g., nonspecific) Mn^{2+}, followed by quantification of the extracted Mn^{2+}. This method is inapplicable, owing to the following reasons. For our EPR samples, the photoactivation medium contains 6−8 Mn/PSII, necessary to achieve adequate occupancy of the high-affinity Mn^{2+} site (dissociation constant of 40−50 μM). As we showed, thawing of these samples after the illumination at −20 °C leads to immediate charge recombination (via Q$_A^-$) that reduces Mn^{3+} to Mn^{2+} and thus renders the specifically bound Mn^{2+} labile at temperatures higher than −10 °C. Owing to its weak binding affinity, the specific Mn^{2+} dissociates during the washing procedure. Three prior studies of the Mn^{2+} stoichiometry required for photoassembly (assayed by the rate and yield of recovery of O$_2$ evolution capacity at room temperature) measured as a function of the concentration of added Mn^{2+} per PSII showed that 1 Mn is taken up in the initial lag phase, corresponding to step 1 (Scheme 2) and 3 Mn are subsequently taken up cooperatively to produce an O$_2$-evolving center (*18, 25, 35*).

In contrast to the nearly equal yields of the photobleaching decay of the Mn^{2+} signal seen in Figure 2A, the saturation level of the Mn^{3+} signals is quite different in the presence and absence of Ca^{2+} in Figure 2B. In the presence of Ca^{2+}, the saturated Mn^{3+} signal intensity is greater by 60% compared to PSII without Ca^{2+}. As we shall show below, this intensity difference can only be explained if the photo-oxidized Mn^{3+} exists in two forms, e.g., *EPR-invisible* Mn^{3+} and *EPR-visible* Mn^{3+}. The addition of Ca^{2+} shifts the equilibrium from an *EPR-invisible* to *EPR-visible* Mn^{3+} and thus results in a greater intensity of the Mn^{3+} signal in Ca^{2+}-containing samples at pH 7.5.

Dissociation Constant of Mn^{2+} at the High-Affinity (Photo-oxidizable) Site in PSII. The shape and intensity of the photo-oxidized Mn^{3+} signal were examined in the range of the Mn^{2+} concentration from 10 to 320 μM (0.5−16 Mn^{2+}/PSII). The Mn^{3+} line shape was found to be invariant (Figure S2 in the Supporting Information), while only the signal intensity increased to a maximum (Figure 3). This behavior suggests that the Mn^{3+} signal corresponds to a unique Mn^{3+} site in PSII and that the population of this site saturates when the Mn^{2+} concentration increases. The concentration dependence was used to estimate the dissociation constant at this site. Because illumination was performed at −20 °C, where diffusion processes are prevented (see above), the measured dissociation constant corresponds to the equilibrium before freezing and illumination, e.g., to the binding of Mn^{2+} in the dark to the photo-oxidizable site in PSII. The concentra-
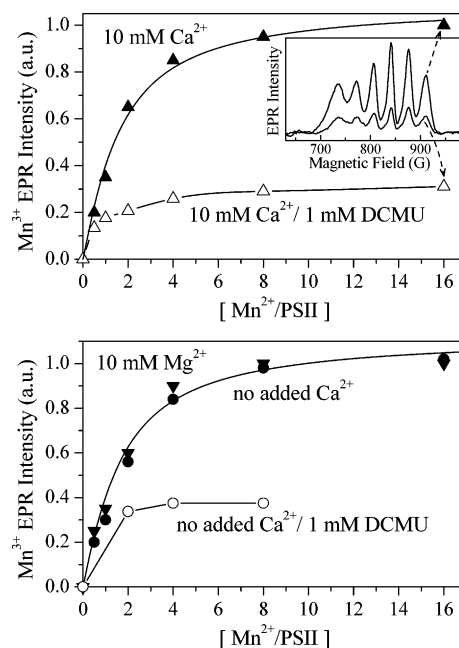

FIGURE 3: Dependence of the light-induced Mn^{3+} EPR signal intensity on the concentration of Mn^{2+} in apo-WOC−PSII in the presence of (▲) 10 mM Ca^{2+}, (△) 10 mM Ca^{2+} and 1 mM DCMU, (●) no added Ca^{2+}, (○) no added Ca^{2+} and 1 mM DCMU, and (▼) 10 mM Mg^{2+}. Assay conditions: 20 μM apo-WOC−PSII, HEPES at pH 7.5; 15 min of illumination at −20 °C. Solid lines are fits assuming one photo-oxidizable Mn^{2+} site per PSII. The fitted dissociation constants for Mn^{2+} are comparable in all three samples with 10 mM Ca^{2+}, 10 mM Mg^{2+}, and no added Ca^{2+} (K_D = 40−50 μM). The inset shows that the Mn^{3+} EPR line shape is identical in the presence of DCMU, while the intensity is reduced to 30%.

tion dependence fits best to a model assuming a single Mn^{2+}-binding site, as shown by the solid-line fits in Figure 3. The best fit gives a dissociation constant K_D = 40−50 μM, which is comparable in all three PSII samples studied, e.g., in the presence of 10 mM Ca^{2+}, 10 mM Mg^{2+}, and with no added Ca^{2+}/Mg^{2+}. We conclude that neither Ca^{2+} nor Mg^{2+} at 10 mM concentrations produces a measurable affect on the Mn^{2+} affinity to apo-WOC−PSII.

Importantly, there is no threshold observed in the concentration dependences in Figure 3, and the Mn^{3+} signal rises linearly, starting from substoichiometric concentrations of Mn^{2+}/PSII. We may conclude that these titration data and the estimated K_D = 40−50 μM correspond to the Mn^{2+} site, which possesses the highest affinity to Mn^{2+}, e.g., the so-called "high-affinity Mn^{2+} site" in PSII (*48*). All other possible Mn^{2+} sites must have a much lower affinity (with K_D > 100 μM) to comply with the observed titration data as can be estimated from the numerical fits.

A Single Photochemical Turnover Forms Mn^{3+}. 3-(3,4-Dichlorophenyl)-1,1-dimethylurea (DCMU) is a well-known inhibitor of the acceptor Q$_B$ site in PSII and was used to restrict the number of light-induced electron turnovers to a single electron. The Mn^{3+} signal generated in the presence of 1 mM DCMU has an identical line shape (inset of Figure 3A) but lower yield (30%) compared to no DCMU samples (parts A and B of Figure 3). Electron recombination from Q$_A^-$ to Mn^{3+} is efficient at −20 °C (*43, 49, 50*) and is the most probable cause of the lower yield of Mn^{3+} in the presence of DCMU. In contrast, when no DCMU is present, the electron may advance to the acceptor Q$_B$ site with a
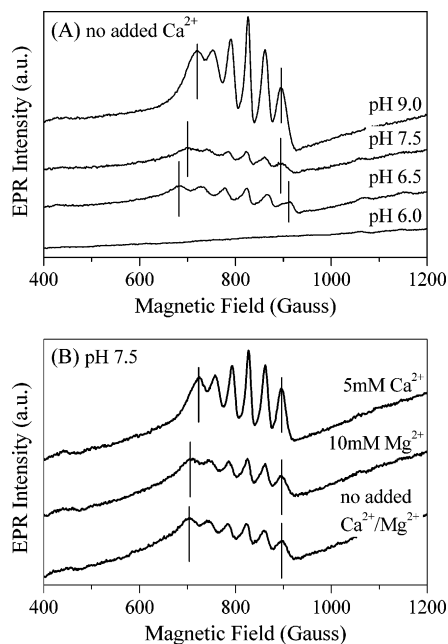
FIGURE 4: Light-induced Mn^{3+} EPR signals in apo-WOC−PSII. (A) pH dependence with no added Ca^{2+} and (B) at fixed pH 7.5, in the presence of 10 mM Ca^{2+} or Mg^{2+}, and with no added Ca^{2+}/Mg^{2+}. All samples contain 24 μM apo-WOC−PSII and 120 μM Mn^{2+} (HEPES at pH 7.5); 15 min of illumination at −20 °C. Vertical lines mark the outer ^{55}Mn hyperfine lines in the spectra.

higher probability (*44*). As a consequence, the probability for the electron recombination process is much lower and the yield of Mn^{3+} is higher. Thus, the invariance of the Mn^{3+} spectral shape upon DCMU addition, upon illumination time (Figure 1), and upon the Mn^{2+} concentration (Figure 3) provides supportive evidence that the observed Mn^{3+} signal corresponds to a single site in PSII and that this site possesses a homogeneous environment.

Influence of pH and Ca^{2+} on the Mn^{3+} Signal. The Mn^{3+} spectra in the pH range of 6−9 and in the presence of added Ca^{2+} or Mg^{2+} are shown in parts A and B of Figure 4, respectively. The Mn^{3+} signals differ noticeably in the center field position (g_{eff}), the resolved ^{55}Mn hyperfine coupling (A_Z), and the signal intensity. The spectral characteristics of the Mn^{3+} signals are summarized in Table 1 and plotted in Figure 5A as g_{eff} versus A_Z at each pH and in the presence and absence of Ca^{2+}. For comparison, the Mn^{3+} signal previously reported in PSII core particles from *Synechocystis* at pH 6.1 (*40*) is also included in Table 1.

Changing the pH from 6.5 to 9.0 produces a monotonic decrease in both g_{eff} and A_Z (Figure 5A). The effect is considerably stronger in the absence of added Ca^{2+}, with g_{eff} decreasing by 0.08 units (1%) and A_Z decreasing by 10 G (22%). The addition of 5−10 mM Ca^{2+} largely suppresses the pH effect on these spectral characteristics and moves both g_{eff} and A_Z to a range of values observed at alkaline pH ≥ 9 without added Ca^{2+}. Identical changes were seen at 5 and 10 mM Ca^{2+}, indicating the complete transformation of the Mn^{3+} spectra (not shown). By contrast, the addition of 10 mM Mg^{2+} produces very little effect on g_{eff} and A_Z, establishing a specific influence by Ca^{2+} (Figure 4B). The Ca^{2+} effect on the spectral properties of Mn^{3+} occurs at the same Ca^{2+} concentration that optimizes the O_2 evolution flash yield during photoactivation experiments (*23, 28*) and also the O_2 activity of the holoenzyme depleted of Ca^{2+} (*30, 31*).

Thus, the present data provide direct evidence that Ca^{2+} binds to its effector site in the dark, before freezing to −20 °C and subsequent photo-oxidation of Mn^{2+}. Furthermore, the significant changes in the spectral parameters of the photo-generated Mn^{3+} indicate that Ca^{2+} binds in close proximity to the photo-oxidizable Mn^{2+} site and affects the ligand-field symmetry of the site.

Figure 5B plots the calculated yield of the light-induced Mn^{3+} centers in the pH range from 6.0 to 9.0. The yield was calculated as the integrated signal intensity under the six-line Mn^{3+} signal, divided by the transition probability μ^2 of the signal at the indicated pH (Table 1). μ^2 was determined using the experimental g_{eff} of the Mn^{3+} signal (the detailed procedure is outlined below and illustrated in parts A and B of Figure 6). Thus, the calculated yield is proportional to the number of *EPR-detectable* Mn^{3+} centers and is independent of the transition probability. The yield is 0% at pH 6.0 and below and grows with increasing pH in a nonmonotonic titration curve, reaching 20−25% at pH 6.5−7.5 and a maximum level (taken as 100%) at pH 9.0. The dependence is not monotonic and extends over a broad pH range, indicating that more than one pK_a equilibrium step is involved. The addition of 10 mM Ca^{2+} (but not Mg^{2+}) appreciably transforms the pH titration curve in Figure 5B, again confirming a specific association of the Ca^{2+}-binding site with the high-affinity Mn^{3+} site.

The Mn^{2+} signal intensity was also measured before and after illumination at −20 °C. The Mn^{2+} signal decreases upon illumination by 30−40% at pH 6.0−6.5 and by 45−65% at pH 7.5 (Figure S1 in the Supporting Information). Although quantitative estimation of Mn^{2+} photoconversion is difficult, the observed pH dependence of the photo-oxidizable Mn^{2+} reveals that a significant and comparable fraction (30−65%) of Mn^{2+} is photo-oxidized in the pH range of 6.0−7.5. The presence of 10 mM Ca^{2+} produces a weak effect on the amplitude of the Mn^{2+} photobleaching, and thus, the number of photo-oxidizable Mn^{2+} is comparable in the absence and presence of Ca^{2+}. At pH 9.0 and higher, no Mn^{2+} signal was detectable in the EPR spectra before or after illumination, and thus, an estimation of the Mn^{2+} photo-oxidation yield was impossible at this pH.

The modest change of Mn^{2+} photobleaching in the pH range 6 to 7.5 stands in marked contrast to the large change in the yield (0−100%) of the EPR-detectable Mn^{3+} produced at these pH values (Figure 5B). At pH 6.0, although a substantial amount of Mn^{2+} is oxidized (30−40%), there is no EPR-visible Mn^{3+} produced. As pH increases, the number of photo-oxidized Mn^{2+} changes only slightly (to a maximum of 65%) but the number of EPR-visible Mn^{3+} increases sharply from 0% at pH 6.0 to 25% at pH 6.5 and then to 100% at pH 9.0. This uncorrelated behavior can only be understood if the Mn^{3+} formed by photo-oxidation exists in a pH-dependent equilibrium of at least two forms, one *low-pH EPR-invisible* form and one *high-pH EPR-active* form . Only the low-pH EPR-invisible Mn^{3+} is photogenerated at pH 6.0 and below, and thus, no EPR signal of Mn^{3+} is observed. At higher pH, the equilibrium gradually shifts to the high-pH EPR-active Mn^{3+} form(s), and thus, the progressively stronger Mn^{3+} EPR signal is found at a comparable level of Mn^{2+} photo-oxidation. The nature of this equilibrium and reason for the inability to detect the low-pH form is discussed later.

Table 1: Spectral Characteristics and the Derived Spin-Hamiltonian Parameters of Mn^{3+} Formed at the High-Affinity Mn^{2+} Site in PSII at Different pH and in the Absence or Presence of Ca^{2+} (10 mM) or Mg^{2+} (10 mM)

	spinach PSII (this paper)[a]							*Synechocystis* PSII[b]
pH	6.5		7.5			9.0		6.1
cofactors	0	Ca^{2+}	0	Mg^{2+}	Ca^{2+}	0	Ca^{2+}	0
g_{eff}	8.196 ± 0.01	8.107 ± 0.005	8.151 ± 0.01	8.142 ± 0.02	8.096 ± 0.005	8.117 ± 0.005	8.080 ± 0.005	8.2
A_Z (Gauss)	45 ± 0.3	35.2 ± 0.3	38.6 ± 0.5	37.6 ± 0.5	34.8 ± 0.3	35.5 ± 0.3	33.6 ± 0.3	44.8
yield of Mn^{3+} (%)[c]	22	19	25	24	48	100	49	
δ (deg)	4.43 ± 0.09	4.11 ± 0.04	4.3 ± 0.06	4.24 ± 0.08	4.06 ± 0.04	4.15 ± 0.04	4.0 ± 0.04	
μ^2	0.3 ± 0.04	0.22 ± 0.04	0.27 ± 0.04	0.25 ± 0.04	0.21 ± 0.04	0.23 ± 0.04	0.20 ± 0.04	
g_Z[d]			1.967 ± 0.01					1.98
D (10^{-4} cm^{-1})			-3.5 ± 0.4					-2.5
E (10^{-4} cm^{-1})	0.32 ± 0.04	0.29 ± 0.04	0.31 ± 0.04	0.31 ± 0.04	0.28 ± 0.04	0.3 ± 0.04	0.28 ± 0.04	0.269
$P\alpha^2$ (10^{-4} cm^{-1})[e]	107 ± 3	83.7	91.6	89.2	82.7	84.3	80.0	111
K_D (μM)[f]			45 ± 5	45 ± 5	45 ± 5			

[a] The mean value in the derived parameters was obtained assuming $\Delta = 20\,000$ cm^{-1}, and the upper and lower error limits correspond to $\Delta = 30\,000$ and $15\,000$ cm^{-1}, respectively. Each parameter represents an average of at least three replicate measurements, with a variation between experiments smaller than the indicated error bars. [b] From ref 40, the assumptions made were $\delta = 0$, $\kappa = 0.5$, and $\lambda/\Delta = 2.5 \times 10^{-3}$ (the later corresponds to $\Delta = 35\,000$ cm^{-1}). [c] The yield of EPR-visible Mn^{3+} was calculated as the integrated intensity of the six-line Mn^{3+} signal normalized by the calculated transition probability μ^2 of that signal. [d] The derived g_Z and D are identical for all Mn^{3+} signals measured in this work. [e] Invariant $\kappa = 0.5$ was assumed in deriving $P\alpha^2$ from the experimental A_Z. [f] Dissociation constant for Mn^{2+} at the high-affinity Mn^{2+} site in PSII.
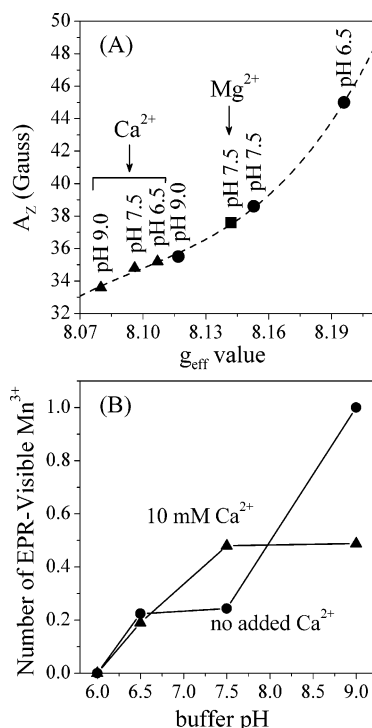

FIGURE 5: (A) Correlation between the effective electron g factor (g_{eff}) and ^{55}Mn hyperfine coupling (A_Z) of the light-induced Mn^{3+} EPR signal observed at different pH (as labeled) with no added Ca^{2+} (●) and in the presence of 5−10 mM Ca^{2+} (▲) or 10 mM Mg^{2+} (■). Each point represents an average of at least three replicate measurements, with a variation between experiments smaller than the size of the symbols. The dashed line is a guide for the eyes. (B) Number of EPR-visible Mn^{3+} (calculated as the integrated intensity of the six-line Mn^{3+} signal normalized by the transition probability μ^2 of that signal) at different pH. The Mn^{3+} yield at pH 9.0 was taken as 100%.

Estimation of the Mn^{3+} Photo-oxidation Yield by EPR Spectral Simulations. The above observation of a pH-dependent interconversion of EPR-visible and -invisible populations of Mn^{3+} was further tested by spectral simulations using the program described by Golombek and Hen-
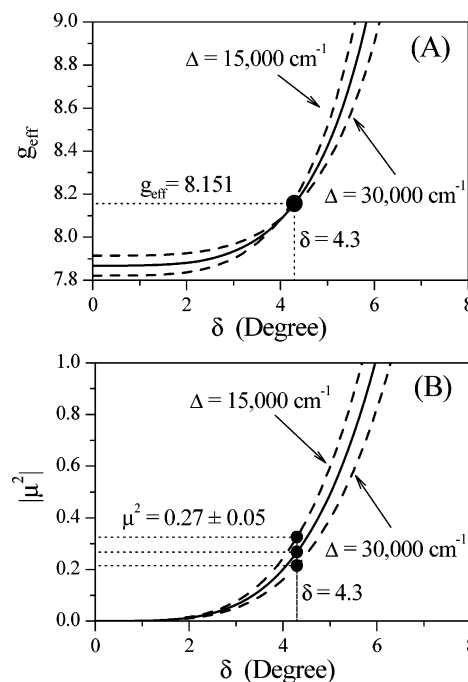

FIGURE 6: Dependence of g_{eff} (A) and μ^2 (B) on the ligand-field rhombicity parameter δ, as calculated using eqs A1−A3 and assuming fixed values for the ligand-field parameters [$\rho = 0.8$ cm^{-1} (76) and $\lambda = +88$ cm^{-1} (57)], while allowing the energy splitting Δ to change: (—) $\Delta = 20\,000$ cm^{-1} and (- - -) $\Delta = 15\,000$ and $30\,000$ cm^{-1}. Horizontal and vertical dashed lines in A demonstrate that the rhombicity $\delta = 4.3°$ is derivable from $g_{eff} = 8.151$ of the Mn^{3+} signal at pH 7.5, and the dashed lines in B show that this derived rhombicity $\delta = 4.3°$ is used to determine the transition probability μ^2 of the Mn^{3+} signal at $g_{eff} = 8.151$.

drich (51). EPR spectral simulations were performed using the parameters from Table 1 (e.g., g_Z, A_Z, D, and E) as obtained from the experimental data as described in the previous section. The simulations are deposited in the Supporting Information (Figure S3). To properly fit the experimental signal intensities, the number of Mn^{3+} centers contributing to the signal at pH 9.0 had to be increased by

Scheme 1:   State Energy Diagram of Mn^{3+} ($3d^4$, ^5D) in an Orthorhombic Ligand Field[a]
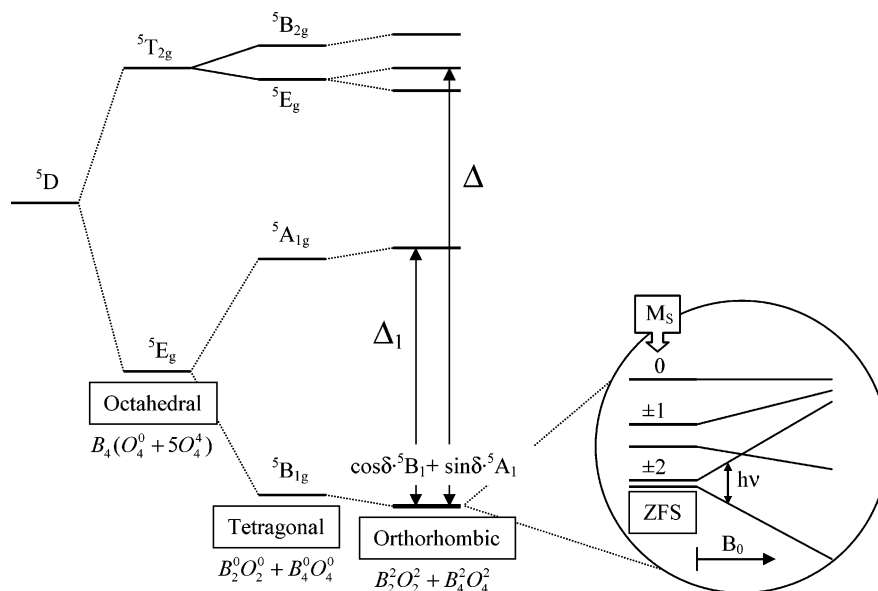
[a] The orthorhombic ligand field mixes the $^5B_1$ and $^5A_1$ states, yielding the ground state (cos $\delta \cdot ^5B_1$ + sin $\delta \cdot ^5A_1$). The inset shows ZFS and Zeeman energy splitting of the ground state for the case of small δ (predominantly $^5B_1$ ground state), which results in $M_S = \pm 2$ levels being the lowest. The EPR transition between the $M_S = \pm 2$ level is detected in parallel-mode EPR as indicated by the transition arrow, $h\nu$.

3-fold relative to the number of Mn^{3+} centers at 6.5. The line shape on the low-field side of the simulated spectrum at pH 9.0 is slightly sharper than the experimental spectrum, indicating additional broadening mechanisms not included in the simulation; however, this feature does not contribute to the prediction of the spin concentration. In summary, the spectral simulations corroborate the ligand-field analysis in the previous section, demonstrating that the observed large change in the Mn^{3+} signal intensity between pH 6.5 and 9.0 corresponds to a change in the number of EPR-active Mn^{3+} species, and it is not attributable to the small change in E/D.

Spin-Hamiltonian Analysis of the Mn^{3+} EPR Spectra. The Mn^{3+} EPR signal at $g_{eff} \sim 8$ is typical of Mn^{3+} ions in approximately axially symmetric ligand fields and corresponds to the transition between the $M_S = \pm 2$ levels of a spin $S = 2$ ground state (40, 52−55). The signal at $g_{eff} \sim 8$ corresponds to a turning point of an overall broad EPR powder line shape from Mn^{3+} complexes whose principal zero-field splitting (ZFS) axis is oriented nearly parallel to the external magnetic field (B_0). Other orientations are mostly unobservable at this (X-band) microwave frequency. Equation A1 (Appendix) describes the center position of the signal (g_{eff}) for the general case of a ligand field with orthorhombic symmetry; g_{eff} is determined by one of the principal values of the intrinsic (Zeeman) g factor (e.g., g_Z that lies along the principal axis Z of the ZFS tensor) and is shifted to higher g values by the presence of a finite orthorhombic ZFS term ($3E^2/D$).

The experimentally resolved ^{55}Mn hyperfine splitting (A_Z) corresponds to the component of the hyperfine tensor along the Z axis of the ZFS tensor, and it can be described by eq A4 (Appendix) derived from the ligand-field theory. The intensity of the Mn^{3+} signal involves three terms: the transition probability μ^2, the number of Mn^{3+} spins, and the experimental parameters involving sample volume, spectrometer conditions, and temperature. In parallel-mode EPR, with the microwave magnetic field B_1 parallel to B_0, the transition probability μ^2 is proportional to E^4/D^2 (eq A2 in

the Appendix) and, therefore, for this transition to be observable, requires a nonzero rhombic component of the ZFS. While it is difficult to assess absolute values for μ^2 from the experimental spectral intensities, it is possible to compare relative μ^2 for two samples provided that other experimental conditions are identical. Thus, the two spectral parameters, g_{eff} and A_Z, and the relative μ^2 intensities can be obtained directly from the experimental Mn^{3+} spectra and then can be used to determine or constrain the spin-Hamiltonian parameters (D, E, g_Z, and A_Z) and to describe the ligand environment and electronic configuration of the ground state of the Mn^{3+}, using the theoretical expressions derived from the ligand-field theory (eqs A3 and A4 in the Appendix).

Ligand-Field Theory Applied to Mn^{3+}. Scheme 1 gives a typical ligand-field diagram for the ^5D atomic state derived from a $3d^4$ electron configuration. The orthorhombic symmetry of the Mn^{3+} ligand field (which is required to observe the $g \sim 8$ signal) results in a ground electronic state (cos $\delta \cdot ^5B_1$ + sin $\delta \cdot ^5A_1$) that is a mixture of $^5B_{1g}$ and $^5A_{1g}$, the ground states that arise in the case of pure axial (tetragonal) symmetry. The $^5B_{1g}$ and $^5A_{1g}$ states correspond to the electronic configurations in which the electronic hole associated with the $3d^4$ orbital configuration of Mn^{3+} occupies the $d_{x^2-y^2}$ orbital or the d_{z^2} orbital, respectively (56). The mixing parameter δ originates from the nonzero orthorhombic ligand-field terms ($B_2^2 O_2^2 + B_4^2 O_4^2$) (57). This δ defines the rhombicity of the ligand field directly in terms of the d orbital mixing, and therefore, it can be used equivalently instead of the rhombic ZFS term E commonly used in the spin-Hamiltonian treatment of the effective "spin-only" ground state.

According to eqs A1 and A3 and at typical ligand-field parameters (summarized in the Appendix), the rhombicity range of $6° < \delta < 84°$ results in $g_{eff} > 9$, which is too large compared to the experimental $g_{eff} = 8.1−8.2$ reported here (Figure 5A). Thus, only $\delta < 6$ or $\delta > 84$ needs to be

considered, which corresponds to either $^5B_1$ or $^5A_1$ being the dominant term in the Mn^{3+} ground state, respectively. For A_Z in the range observed here, 35−45 G (Figure 5A), only the lower range $\delta < 6$ is possible (i.e., predominantly the $^5B_1$ ground state), because the $^5A_1$ state typically exhibits A_Z as high as 100 G (*40*). Parts A and B of Figure 6 present g_{eff} and μ^2 calculated using eqs A1−A3 for the range of the rhombicity parameter $\delta = 0-8°$. In these calculations, we allowed the ligand-field energy splitting Δ to the excited $^5T_{2g}$ states (Scheme 1) to change 2-fold, while fixed values for the intrinsic atomic parameters (spin−spin coupling $\rho = 0.8$ cm^{-1}, and spin−orbit coupling $\lambda = 88$ cm^{-1}) were used. Indeed, only a small variation of these atomic parameters occurs upon the formation of a complex. For example, the spin−orbit coupling parameter λ may be reduced by covalency by at most 10−20% from its atomic value by the addition of six oxygen or nitrogen ligands (*58*). By contrast, the ligand-field energy splitting Δ varies over a significant range of 15 000−30 000 cm^{-1} for five- and six-coordinate Mn^{3+} complexes and tends to the lower value in complexes with all oxygen ligands (*59*). Therefore, three different Δ values were considered in the simulation given in Figure 6 to cover a maximum range. All three curves with different Δ run closely parallel and demonstrate the degree of uncertainty in the fits. The dependence of g_{eff} on δ is monotonic and thus allows one-to-one mapping of the experimental g_{eff} into the rhombicity parameter δ. The horizontal and vertical dotted lines in Figure 6A illustrate how $g_{\text{eff}} = 8.151$ (of the Mn^{3+} at pH 7.5) projects into a narrow range of $\delta = 4.3 \pm 0.1°$ (the indicated error arises from uncertainty in the range of Δ). The derived rhombicity δ together with the maximum range of Δ can then be used to determine the spin-Hamiltonian parameters (D, E, and g_Z) and the transition probability μ^2 of the Mn^{3+} signal. This is shown by the dotted lines in Figure 6B to demonstrate how the transition probability $\mu^2 = 0.27 \pm 0.05$ results from $\delta = 4.3$. The derived spin-Hamiltonian parameters of these and other Mn^{3+} signals are summarized in Table 1.

Analysis of the ^{55}Mn Hyperfine Interaction. The calculated change in A_Z (eq A4) over the expected range of the rhombicity parameter $0 < \delta < 6$ (at fixed Δ) is only 1%, and therefore, changes in δ alone cannot explain the 22% decrease in the hyperfine splitting upon increasing the pH from 6.5 to 9 ($A_Z = 45-35.5$ G). For Δ values from 30 000 to 15 000 cm^{-1}, which covers virtually all known five- and six-coordinate complexes, the maximum change in A_Z is calculated to be only 2.5 G. Therefore, a change in Δ can also be excluded as a significant source of the observed variation in A_Z.

The leading terms in the expression for A_Z (eq A4) are $-P\alpha^2\kappa$ and $P\alpha^2/7$. These terms account for the isotropic and anisotropic contributions to the ^{55}Mn hyperfine tensor, respectively. To evaluate each term individually requires knowledge of the complete ^{55}Mn hyperfine tensor. However, only one of the principal components of the hyperfine tensor (viz., A_Z) is resolved in the Mn^{3+} EPR spectra, and therefore, we have no direct means to discriminate between isotropic and anisotropic contributions to A_Z and to determine which term of the two is responsible for the A_Z variation observed in our experimental data. Hence, in the following analysis, we resort to a comparison with other experimental data of
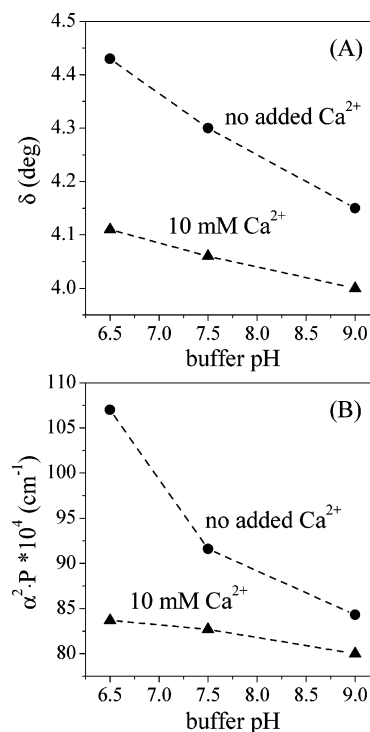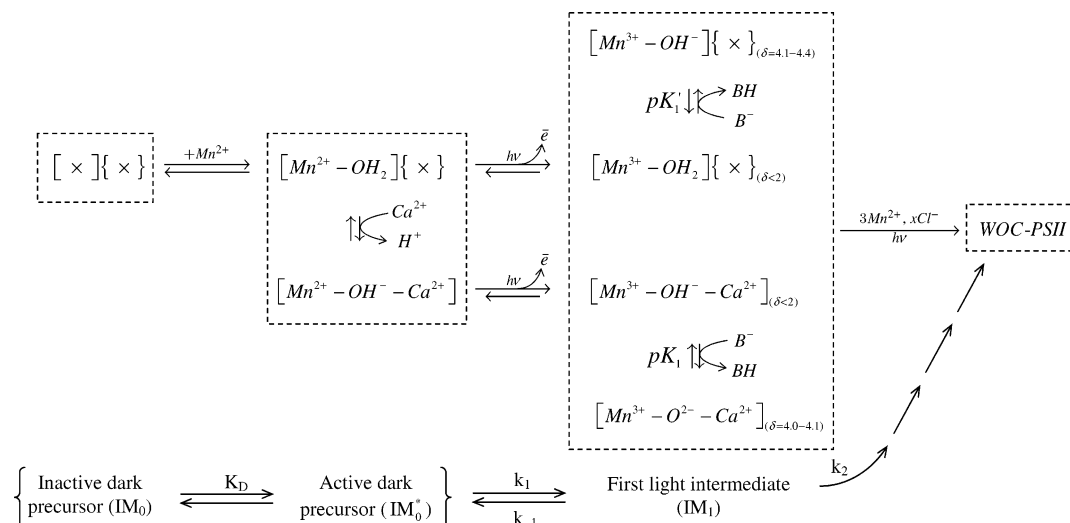

FIGURE 7: pH dependence of the derived ligand-field parameters of the photo-oxidized Mn^{3+} in PSII. (A) Ligand-field rhombicity δ and (B) electron spin density $P\alpha^2$, in the presence of 10 mM Ca^{2+} and no added Ca^{2+}.

related model complexes and also to the ligand-field theory for insight into the origin of the A_Z change.

The factor $P\alpha^2$ scales both the isotropic and anisotropic hyperfine terms in the expression for A_Z. Here, $P = 2\beta_e\beta_N g_e g_N \langle r^{-3}\rangle$, with r being the electron−nucleus distance, accounts for changes in the spatial extent of the unpaired electron spin density in Mn orbitals as a consequence of electron repulsions from the ligands, and $\alpha^2 \leq 1$ is the metal−ligand covalency factor. Another unknown is κ, a dimensionless parameter accounting for nonzero spin density at the ^{55}Mn nucleus, arising from an admixture of excited electronic configurations having unpaired s electron densities. The theoretical prediction of κ is a rather difficult task; however, quite interestingly, κ is observed experimentally to be nearly constant for a given oxidation state of the ion and at different ligand configurations (*57*, *60*). The experimental value $\kappa = 0.52$ was determined for Mn^{3+} in TiO$_2$ (*56*). We accept this value for the purpose of our analysis and assume $\kappa = 0.5$ being a constant and thus focus on changes to $P\alpha^2$ as the most significant source of the change in A_Z. The derived $P\alpha^2$ and other ligand-field parameters for the Mn^{3+} at different pH and Ca^{2+} concentrations are summarized in Table 1. Two of the derived ligand-field parameters (viz. δ and $P\alpha^2$) are found to be most responsive to changes in pH and Ca^{2+} addition, and these are plotted in parts A and B of Figure 7, respectively.

DISCUSSION

Binding Affinity of Mn^{2+} for the High-Affinity Site in PSII. The photoconversion yield of the Mn^{3+} signal is a maximum at −20 °C with no evidence for decay or spectral changes in time for more than 15 min at this temperature. The Mn^{3+} exhibits uniform spectral properties, reflecting a single

Scheme 2:   Proposed Intermediates in the First Steps of Photoactivation[a]

$$\left[\,\times\,\right]\{\,\times\,\} \underset{}{\overset{+Mn^{2+}}{\rightleftharpoons}} \left[Mn^{2+}-OH_2\right]\{\,\times\,\} \overset{hv}{\underset{\bar{e}}{\longrightarrow}} $$

$$\left[Mn^{3+}-OH^-\right]\{\,\times\,\}_{(\delta=4.1-4.4)}$$

$$pK_1' \,\updownarrow\!\!\updownarrow\; \overset{BH}{\underset{B^-}{}}$$

$$\left[Mn^{3+}-OH_2\right]\{\,\times\,\}_{(\delta<2)}$$

$$\updownarrow\!\!\updownarrow\; \overset{Ca^{2+}}{\underset{H^+}{}}$$

$$\left[Mn^{2+}-OH^--Ca^{2+}\right] \overset{hv}{\underset{\bar{e}}{\longrightarrow}} \left[Mn^{3+}-OH^--Ca^{2+}\right]_{(\delta<2)}$$

$$pK_1 \,\updownarrow\!\!\updownarrow\; \overset{B^-}{\underset{BH}{}}$$

$$\left[Mn^{3+}-O^{2-}-Ca^{2+}\right]_{(\delta=4.0-4.1)}$$

$$\overset{3Mn^{2+},\,xCl^-}{\underset{hv}{\longrightarrow}} \; WOC\text{-}PSII$$

$$\left\{ \begin{array}{c} \text{Inactive dark} \\ \text{precursor (IM}_0) \end{array} \right. \underset{}{\overset{K_D}{\rightleftharpoons}} \left. \begin{array}{c} \text{Active dark} \\ \text{precursor (IM}_0^*) \end{array} \right\} \underset{k_{-1}}{\overset{k_1}{\rightleftharpoons}} \begin{array}{c} \text{First light intermediate} \\ \text{(IM}_1) \end{array} \overset{k_2}{\nearrow}$$

[a] Protein-derived and nonchanging water ligands to Mn^{2+}/Mn^{3+} are not shown. Brackets [ ] and { } represent the high-affinity Mn^{2+} site and the Ca^{2+} effector site of apo-WOC−PSII, respectively. [×] and {×} represent unoccupied sites. The species $[Mn^{3+}OH_2]$ and $[Mn^{3+}(OH^-)Ca^{2+}]$ are EPR-silent. The subscript δ indicates the rhombicity of the ligand field of Mn^{3+} as determined from the EPR measurements: $\delta < 2$ for the EPR-silent Mn^{3+} species, and $\delta \sim 4.3$ for the EPR-detectable Mn^{3+} species. A range of δ is shown for the Mn^{3+} species, which show pH-induced changes in the rhombicity of the ligand field. At the bottom, the correspondence is shown to the kinetic intermediates (IM_n) of the minimal kinetic model (18, 19).

binding site with a homogeneous environment. The titration curves for Mn^{3+} (Figure 3) fit well to a single-site-binding model for the Mn^{2+} precursor characterized by a dissociation constant $K_D = 40-50 \ \mu M$ at pH 7.5. The present method measures the reversible binding of the photo-oxidizable Mn^{2+} in the dark (e.g., without interference from other light-dependent reactions at this site, such as Mn^{2+} light-induced oxidation and subsequent dissociation as Mn^{3+}), and thus, it gives a true measure of the equilibrium dissociation constant for this Mn^{2+}. Within the 10% error of the method, the same K_D is found in the absence and presence of up to 10 mM divalent cations, indicating that neither Ca^{2+} nor Mg^{2+} compete efficiently with Mn^{2+} for binding to the high-affinity Mn^{2+} site, as was previously known (29, 61−63). This Mn^{2+} site possesses the highest affinity for apo-WOC−PSII, and therefore, we associate this photo-oxidizable site with the previously described "high-affinity Mn^{2+} site" involved in electron donation (48, 62) and photoactivation (22, 64).

There is widespread disagreement in the literature on the binding strength of the high-affinity Mn^{2+} site. Our K_D compares very well with two of the numerous reports in the literature, 40 μM (65) and 51 μM (22), but differs substantially from other measurements involving nonequilibrium electron-transfer rate measurements that require photo-oxidation of multiple Mn^{2+} ions. For example, $K = 10 \ \mu M$ at pH 5−6 and 0.5 μM at pH 7−8 were found by monitoring Mn^{2+}-dependent electron transport (66); $K < 1 \ \mu M$ by monitoring Mn^{2+} competition with a nonphysiological electron donor (DCIP) (62, 67); and $K < 25 \ \mu M$ by reduction of $Y_Z^·$ by Mn^{2+} using multiple laser flashes (38).

pH Equilibria of Mn^{3+} Species. The substantial change in the ligand environment of the high-affinity Mn^{3+} ion with pH and Ca^{2+} addition may involve three contributions: (1) deprotonation of a ligand (protein amino acid or coordinated water), (2) deprotonation of remote protein amino acid groups leading to a global protein conformational change that may alter the immediate ligand structure, and (3) binding of a

new ligand (protein or solvent derived). In principle, any one or a combination of these mechanisms may be responsible for the observed pH effects on the Mn^{3+} in PSII. The present data alone do not allow an unambiguous discrimination between these mechanisms. However, a quantitative determination of the strength and symmetry of the perturbation to the ligand field of Mn^{3+} that is responsible for the observed effects can be obtained, as described next.

The observation of a nearly pH-independent loss of Mn^{2+} signal intensity upon illumination at −20 °C and a highly pH-dependent yield of EPR-detectable Mn^{3+} leads us to conclude that Mn^{3+} is generated in equilibrium between two forms: a low-pH EPR-invisible Mn^{3+} and a high-pH EPR-active Mn^{3+}. The reason that the low-pH Mn^{3+} is EPR-undetectable can be due to either too large heterogeneity of the Mn^{3+} ligand field or too small or too large ligand-field rhombicity. Heterogeneity implies significant broadening in the EPR line shape, which makes the signal undetectable. Too small rhombicity ($\delta < 2$) gives a transition probability that is very weak ($\mu^2 = 0.01$), and thus, the signal is masked by the stronger signal because of the high-pH EPR-active Mn^{3+} that is more rhombically distorted ($\delta \sim 4.3$, and $\mu^2 = 0.27$). On the other hand, too large rhombicity ($\delta > 8$) results in ZFS between the $M_S = \pm 2$ level that is greater than the EPR quantum ($3E^2/D > hv_0$), and therefore, such a species would be undetectable at the X-band EPR frequency, $v_0 \sim$ 9 GHz. In either case, it may be concluded that the equilibrium (low-pH Mn^{3+} ↔ high-pH Mn^{3+}) is associated with a significant change in the symmetry of the ligand field at the Mn^{3+} site, such as seen upon direct modification of the inner ligand shell (57, 68).

Our proposed model for the equilibrium between the low- and high-pH Mn^{3+} forms is shown in Scheme 2 (see "first light intermediate IM_1"). It involves proton ionization from one of the inner ligands to Mn^{3+} here postulated to be a water molecule, e.g., $[Mn^{3+}(OH_2)]\{\times\} \leftrightarrow [Mn^{3+}(OH^-)]\{\times\}$ in the absence of Ca^{2+}, where the brackets [ ] symbolize the

high-affinity site in PSII and {×} symbolizes an unoccupied Ca^{2+} effector site. Although the molecular identity of the ionizable ligand has not been uniquely identified in our work, it is most likely a water ligand. The ionization state of the other ligands, both protein derived and other water molecules, is not specified as they are unknown. The equilibrium involved in the deprotonation of the water ligand bound to the Mn^{3+} is also shown for the case with Ca^{2+} bound to its effector site, e.g., [Mn^{3+}(OH$^-$)Ca^{2+}] ↔ [Mn^{3+}(O^{2-})Ca^{2+}], where (on the basis of several lines of evidence described below and also in section *Strong Coupling between Mn^{3+} and Ca^{2+}*) we postulate that Ca^{2+} at its effector site shares the bridging (hydroxo) ligand with Mn^{3+} and causes deprotonation of this ligand. The ionization state of the water ligand is postulated to be controlled by a nearby base B$^-$ (identity unknown), which serves as an immediate proton acceptor with a pK_a that depends upon the occupancy of the Ca^{2+} effector site (pK_1 or pK_1') (*19*).

In Scheme 2, the photoactive dark precursor IM$_0^*$ is symbolized as [Mn^{2+}(OH$_2$)]{×} when the Ca^{2+} site is unoccupied. The pK_a of water bound to free Mn$_{aq}^{2+}$ in solution is 10.5 and may differ slightly (by 1−2 pK units) for [Mn^{2+}(OH$_2$)] at the high-affinity site. This pK_a is likely to decrease when Ca^{2+} binds at its effector site coupled to the [Mn^{2+}(OH$_2$)] site. Therefore, when the Ca^{2+} site is occupied, the photoactive dark precursor is represented by [Mn^{2+}(OH$^-$)Ca^{2+}]. Upon illumination at −20 °C, the photoactive dark precursors are oxidized to produce [Mn^{3+}(OH$_2$)]{×} and [Mn^{3+}(OH$^-$)Ca^{2+}], respectively. These two intermediates are EPR-invisible but can advance to the EPR-detectable forms: [Mn^{3+}(OH$^-$)]{×} and [Mn^{3+}(O^{2-})Ca^{2+}], upon ligand deprotonation. Proton ionization is facilitated by an amino acid base (B$^-$ in Scheme 2) (*19*). Because global pH equilibrium cannot be achieved at −20 °C, the proton diffusion can only occur to this nearby amino acid base and only when this base is deprotonated before freezing (i.e., B$^-$). Thus, the resulting distribution between the EPR-invisible and the EPR-detectable Mn^{3+} species is determined by the pK_a of this amino acid residue (pK_1 or pK_1').

Coordination Number and Geometry of the EPR-Detectable Mn^{3+} Species. The lack of an EPR signal from the low-pH [Mn^{3+}(OH$_2$)]{×} photoproduct allows for an unobstructed measurement of the spectroscopic characteristics of the high-pH form [Mn^{3+}(OH$^-$)]{×} over the pH range of 6.5−9.0 (Figures 4 and 5A and Table 1). Under all examined conditions of pH and Ca^{2+}/Mg^{2+} concentrations, the ground state of the EPR-visible Mn^{3+} remains the high-spin $S = 2$ electronic configuration with spatial symmetry $^5B_1$ (e.g., with the "hole" residing in the d$_{x^2-y^2}$ orbital) and with only ca. 0.5% admixture of the $^5A_1$ state. The $^5B_1$ electronic state is the usual ground state for ligand geometries, including five-coordinate square pyramidal complexes, six-coordinate tetragonally elongated complexes, and their rhombically distorted variants. This ground-state excludes any geometry that places the d$_{z^2}$ orbital as the lowest unoccupied orbital among the 3d set, thus eliminating six-coordinate tetragonally compressed structures, most five-coordinate trigonal bipyramid structures, and trigonal structures of lower coordination number. The $^5B_1$ electronic ground state was also previously assigned to the photoinduced Mn^{3+} formed in the high-

affinity site of *Synechocystis* sp. pcc 6803 PSII core complexes (*40*). When compared at similar pH (6.5), the Mn^{3+} signals in spinach and *Synechocystis* PSII particles show very similar spectral characteristics (Table 1). The effects of different pH and Ca^{2+} addition were not reported for *Synechocystis* by these authors.

Mechanism of the Spectral Changes of the EPR-Detectable [Mn^{3+}(OH$^-$)]{×} Species. In the absence of Ca^{2+}, the high-pH form [Mn^{3+}(OH$^-$)]{×} shows observable changes in ligand-field symmetry ($\delta = 4.4-4.1°$) over a pH range of 6.5−9.0. These changes are however modest compared to much larger changes induced by deprotonation of the direct ligand to Mn^{3+} during the conversion from the low-pH [Mn^{3+}(OH$_2$)] with $\delta < 2$ or $\delta > 8$ to the high-pH [Mn^{3+}(OH$^-$)] with $\delta \sim 4$. In contrast to δ, the ^{55}Mn hyperfine coupling in the high-pH form decreases significantly by 22% in the pH range of 6.5−9.0 ($A_Z = 45-35.5$ G), indicating a major change to the coordination shell of [Mn^{3+}(OH$^-$)]{×}. As discussed above, this significant decrease in the magnitude of A_Z cannot be explained by a very modest change in δ (4.1−4.4°) nor by changes in the ligand-field energy splitting Δ, over this pH range (refer to eq A4). This leaves only contributions to A_Z arising from changes in a product $P\alpha^2$, which has the pH dependence as shown in Figure 7B (κ does not vary appreciably as discussed above).

The observed 22% decrease in A_Z over the pH range of 6.5−9.0 is in fact opposite in sign to that expected if one of the ligands to Mn^{3+} is deprotonated at high pH. Although to our knowledge there are no data in the literature describing the effects of coordination changes to A_Z (^{55}Mn) for Mn^{3+} complexes, the effect of ligand deprotonation on the hyperfine coupling is well-established for analogous Cu^{2+} complexes.[2] It was shown that deprotonation of one water ligand in the aqua complex *increases* the ^{63}Cu hyperfine coupling by 13% from $A_Z = 143$ to 161 G (*69, 70*), while deprotonation of an imidazole ligand *increases* the isotropic hyperfine coupling by 6% from $a_{iso} = 72.7$ to 77.2 G (*71*). In both of these examples, the observed increase in hyperfine coupling can be understood because of either an increase in electron repulsion from the anionically charged ligand (this results in contraction of the d orbitals and thus an increase of P) or decreased covalency of the ligands (increase of α^2).

To account for the 22% decrease in $P\alpha^2$ for [Mn^{3+}(OH$^-$)]{×} (Figure 7B) upon increasing the pH, we postulate one or both of the following reasons. The global pH-dependent protein conformational changes may induce a local change in the inner coordination shell of Mn^{3+}. This change may involve a gradual displacement of one of the direct ligands to Mn^{3+}, which results in a longer (on average) Mn−ligand bond and a weaker electron repulsion within the occupied d orbitals of Mn^{3+}. It is expected then that the size of the d orbitals must increase and thus P must decrease. Alternatively, a pH-induced conformation change may involve the rotation of a π-donor ligand to Mn^{3+}, causing the Mn−ligand covalency to increase and thereby α^2 to decrease.

---

[2] Cu^{2+} is a good electronic model for Mn^{3+}. It has a d^9 electron configuration with the hole residing in d$_{x^2-y^2}$ orbital. It typically occurs in an octahedral ligand environment having a $^2B_{1g}$ ground state (the same as Mn^{3+}). The ligand-field expressions for the electron g tensor and Cu hyperfine tensor are also quite similar to the expressions for Mn^{3+} (*56*).

We note also that the observed changes of g_{eff} and A_Z (Figure 4A) over the pH range of 6.5−9.0 are not discrete but rather vary continuously for the EPR-detectable $[Mn^{3+}(OH^-)]\{\times\}$ species, so that the EPR spectrum at pH 7.5 cannot be simulated as a weighted sum of the spectra at pH 6.5 and 9.0 (not shown). This behavior indicates the possibility of a continuous set of geometry changes in the inner ligand structure of $[Mn^{3+}(OH^-)]\{\times\}$ over this pH range, possibly induced by coupling to other degrees of freedom, such as protein conformational changes or hydrogen bonding of the second shell ligands.

Strong Coupling between Mn^{3+} and Ca^{2+}. The binding of Ca^{2+} at its effector site results in a greatly weakened pH dependence of the Mn^{3+} spectral parameters, with δ becoming more uniform (4.05 ± 0.05) and A_Z becoming smaller and with greatly reduced variation (35.2−33.6 G) in the pH range of 6.5−9.0. Importantly, both δ and A_Z of $[Mn^{3+}-(O^{2-})Ca^{2+}]$ approximate to those observed for $[Mn^{3+}-(OH^-)]\{\times\}$ at very high pH $\geq$ 9 (Figure 5A). Thus, Ca^{2+} binding induces structural changes in the first coordination shell of $[Mn^{3+}(OH^-)]$ that are equivalent to those induced by alkaline pH in the absence of Ca^{2+}. We suggest that Ca^{2+} binding induces a proton ionization from a water ligand in the coordination shell of Mn^{3+} and also organizes the coordination shell to make it more uniform and less susceptible to global protein conformational changes induced by pH.

Further evidence for this strong interaction comes from the pH titration curve for the intensity of the EPR-detectable Mn^{3+}, which simplifies to a two-state equilibrium that saturates above pH 7.5 (Figure 5B). The simplest interpretation of these spectral and population changes is that Ca^{2+} directly modifies the inner coordination shell of Mn^{3+} through binding to an ionizable ligand. As depicted in Scheme 2, Ca^{2+} is proposed to induce the ionization of a second water ligand bound to Mn^{3+} or, more plausibly, a second ionization of the bridging hydroxo ligand, $[Mn^{3+}(OH^-)-Ca^{2+}] \leftrightarrow [Mn^{3+}(O^{2-})Ca^{2+}]$, resulting in a bridging oxide ion. Ionization of a second bridging water to yield $[Mn^{3+}-(OH^-)_2Ca^{2+}]$ cannot be excluded on the basis of the EPR data, although the larger size and ionic bonding properties of calcium dictate that only a single bridging ligand should exist. Because this species is obtained by photo-oxidation at −20 °C, where Ca^{2+} diffusion is frozen-out, the associated dark precursor must be $[Mn^{2+}(OH^-)Ca^{2+}]$, with Ca^{2+} bound to its effector site in the dark before the photochemical turnover. Ionization of the water ligand is coupled to the availability of a local base, B^-, with $pK_a \sim 6.7$, as can be estimated from the titration curve in Figure 5B.

The Role for Ca^{2+} in Photoassembly of the WOC. The proposed intermediates for the initial steps in photoassembly of the WOC inorganic cluster in PSII are summarized in Scheme 2. The intermediates are organized into three categories to enable the ease of comparison with the minimal kinetic model, which is deduced from the previous kinetic work (eq 2 and reproduced at the bottom of Scheme 2). The dark precursor of the photoactivation reaction is represented by two states: inactive IM_0 precursors and active IM_0^* precursors, respectively. Only active precursors have Mn^{2+} bound at the high-affinity site and thus are ready for photochemical turnover to produce the first light-induced

Mn^{3+} intermediate (IM_1). Binding of Ca^{2+} to its effector site exerts no measurable influence on the binding affinity of the first Mn^{2+} (at the so-called high-affinity Mn site) and is not required for binding and photo-oxidation of the high-affinity Mn^{2+} (see the top branch in Scheme 2). However, Ca^{2+} can bind in the dark (before the first photochemical event) to form the coupled dark precursor $[Mn^{2+}(OH^-)Ca^{2+}]$ (the bottom branch in Scheme 2). This coupled precursor is easier to oxidize compared to $[Mn^{2+}(OH_2)]$ alone. Moreover, it produces the light intermediate $[Mn^{3+}(OH^-)Ca^{2+}]$, which is kinetically more stable against decay by charge recombination with Q_A^-. Both of these factors contribute to improving the quantum efficiency of the formation of the first light-induced intermediate IM_1.

The model proposed in Scheme 2 is consistent with the previous photoactivation kinetic model, which revealed evidence for positive cooperativity between Mn^{2+} and Ca^{2+} (*18*). Maintenance of an optimal concentration ratio of Mn^{2+} and Ca^{2+} in the photoactivation medium was shown to be essential to avoid excessive photoinhibition during photoactivation and thus to achieve a high yield of reconstituted WOC−PSII (*22, 28*). Furthermore, at this optimal Mn^{2+}/Ca^{2+} ratio, the yield of reconstituted WOC−PSII was observed to increase in parallel with the rate of the first photo-oxidation step as the concentration of Mn^{2+} is increased (*25*). It was inferred that the majority of photoinhibition damage occurs during the initial k_1 step and that enhancement in the quantum efficiency during this step helps to reduce the photoinhibition damage. Accordingly, in Scheme 2, Ca^{2+} performs its protective role by forming a bridged dark precursor $[Mn^{2+}-(OH^-)-Ca^{2+}]$, which is more efficient in photo-oxidation to Mn^{3+} in IM_1. Ca^{2+} binding enables this by inducing proton ionization of a (water) ligand bound to Mn^{2+}, which thus suppresses the recombination reaction and enables an efficient rate of photoassembly.

When Ca^{2+} is absent during photoactivation, the apo-PSII−WOC can photo-oxidize as many as 20 Mn^{2+} ions per reaction center but it does not form a catalytically functional WOC (*72*). We suggest that formation of $[Mn^{3+}(O^-)Ca^{2+}]$ at the IM_1 level, followed by a slow dark protein conformational change (*25*), is an essential step in templating the system for the subsequent cooperative photo-oxidation of the remaining 3 Mn^{2+} ions in rapid succession in a single kinetically unresolved step to form a catalytically active WOC−PSII (*18*). We suggest that the oxide bridge of $[Mn^{3+}(O^-)Ca^{2+}]$ is a critical element for this cooperative process, in which its tetrahedral (sp^3 hybridized) lone pairs could serve as a coordination site for binding of additional Mn^{2+} ions and facilitate their assembly into the spin-coupled oxo-bridged tetramanganese cluster following photo-oxidation.

The proposed oxo-bridging geometry of the IM_1 intermediate, $[Mn^{3+}(O^{2-})Ca^{2+}]$, in the photoactivation reaction can be compared to the recent structural models of the intact PSII−WOC cluster derived from single-crystal Mn EXAFS or XRD studies that are depicted in Chart 1 (*9, 13*). D1-Asp-170 is known to ligate to the high-affinity Mn^{2+} ion that is the first Mn ion that contributes to the assembly of the Mn_4Ca cluster (*40, 73, 74*). The XRD data reveal that this Mn site corresponds to the Mn ion that lies external to the Mn_3Ca subcluster (*13*), e.g., the left most positioned Mn in each structure shown in Chart 1. From the four structures

shown, only two models, 1 and 4, place Ca^{2+} in a bridging position to Mn at the high-affinity site. Assuming that the [Mn^{3+}(O^{2-})Ca^{2+}] core that forms at the IM$_1$ assembly level serves as a template for binding the remaining three Mn^{2+} ions and that the Ca^{2+} ion does not migrate upon the formation of the fully active WOC cluster during the photoactivation reaction, then only structural models 1 and 4 in Chart 1 are compatible with the photoactivation results reported here.

ACKNOWLEDGMENT

APPENDIX: SPIN HAMILTONIAN OF MN^{3+} IN THE ORTHORHOMBIC LIGAND FIELD

Spectral Characteristics of the Mn^{3+} EPR Signal. The center position of the Mn^{3+} signal is described by an effective g factor

$$g_{\text{eff}} = 4g_Z\left[1 + \frac{(3E^2/D)^2}{(h\nu_0)^2 - (3E^2/D)^2}\right]^{1/2} \quad \text{(A1)}$$

based on published expressions (57). Here, D and E are the axial and rhombic ZFSs for the S = 2 ground state; g_Z is the true (Zeeman) electronic g factor along the direction of the principal ZFS axis; ν_0 is the microwave frequency; and h is Planck's constant. In addition, the Mn^{3+} signal is split into six lines because of the ^{55}Mn hyperfine interaction (the splitting corresponds to the hyperfine component along the z direction, A_Z). Importantly, the transition probability of the Mn^{3+} signal depends strongly upon the ligand-field rhombicity

$$|\mu|^2 \sim \frac{(g_Z)^2(3E^2/h\nu_0D)^2}{2 + 2\exp\left(\frac{3D}{kT}\right) + \exp\left(\frac{4D}{kT}\right)} \quad \text{(A2)}$$

where the temperature factor is also included. Thus, the signal intensity varies as E^4/D^2, and nonzero rhombicity is absolutely required to observe the signal. However, at very large E (such that $3E^2/D > h\nu_0$), the ZFS between electronic levels $M_S = \pm 2$ becomes larger than the microwave quantum and the transition cannot be detected using EPR at ν_0 frequency. In summary, two spectral parameters (g_{eff} and A_Z) and the integrated EPR intensity ($I \sim N\mu^2$, with N being the number of spins in the sample) can be measured from the experiment. These experimental parameters can be related to the ligand-field terms to arrive at a description of the number of ligands and the symmetry of the ligand field that they impose around the Mn^{3+} and the relative ligand-field strength.

Interpretation of Spin-Hamiltonian Parameters in Terms of the Mn^{3+} Electronic Structure. The ^{5}D (S = 2) electronic ground term of the Mn^{3+} ion that originates from the 3d^4 configuration splits into a 3-fold orbitally degenerate state ^{5}T$_{2g}$ and a 2-fold orbitally degenerate state ^{5}E$_g$ when an octahedral ligand field is present (57) (Scheme 1). The orbital degeneracy of the ground term ^{5}E$_g$ is removed by the tetragonal and orthorhombic distortions of the ligand field to give the ground state (cos δ·^{5}B$_1$ + sin δ·^{5}A$_1$), where δ is a state mixing parameter. General expressions relating

the spin-Hamiltonian parameters to the electronic state configuration were previously derived for the electronically equivalent case of Cr^{2+} (75)

$$D = -3\left(\rho + \frac{\lambda^2}{\Delta}\right)\cos 2\delta$$

$$E = \sqrt{3}\left(\rho + \frac{\lambda^2}{\Delta}\right)\sin 2\delta$$

and

$$g_X = g_e - 2\frac{\lambda}{\Delta}(\cos \delta - \sqrt{3}\sin \delta)^2$$

$$g_Y = g_e - 2\frac{\lambda}{\Delta}(\cos \delta + \sqrt{3}\sin \delta)^2$$

$$g_Z = g_e - 8\frac{\lambda}{\Delta}\cos^2 \delta \quad \text{(A3)}$$

where (g_X, g_Y, and g_Z) are the three components of the intrinsic g tensor; g_e is the free electron g factor (2.0023); ρ is the spin−spin coupling constant (0.8 cm^{-1} for Mn^{3+}) (76); λ is the spin−orbit coupling constant (+88 cm^{-1} for free Mn^{3+}) (57); Δ is the energy gap to the excited ligand-field state ^{5}T$_{2g}$ (typically 18−25 000 cm^{-1}) (58, 59). On the basis of the general solutions for the hyperfine spin-Hamiltonian provided by Abragam and Pryce (see eq 3.7 in ref 77), we derived the expressions in (A4) for the ^{55}Mn hyperfine tensor of Mn^{3+} applicable to the particular case of orthorhombic symmetry. These expressions take into account the effects of the rhombic ligand field, spin−orbit coupling, spin polarization, and metal−ligand covalency

$$A_X = -P\Big(\alpha^2\kappa - 3\alpha^2\xi(\cos 2\delta - \sqrt{3}\sin 2\delta) +$$
$$\frac{2\lambda}{\Delta}(\cos \delta - \sqrt{3}\sin \delta)^2\Big)$$

$$A_Y = -P\Big(\alpha^2\kappa - 3\alpha^2\xi(\cos 2\delta + \sqrt{3}\sin 2\delta) + \frac{2\lambda}{\Delta}(\cos \delta +$$
$$\sqrt{3}\sin \delta)^2\Big)$$

$$A_Z = -P\Big(\alpha^2\kappa + 6\alpha^2\xi \cos 2\delta + \frac{8\lambda}{\Delta}\cos^2 \delta\Big) \quad \text{(A4)}$$

where $P = 2\beta_e\beta_N g_e g_N\langle r^{-3}\rangle$ is the fundamental electron nucleus interaction scaled by the inverse cube of r, the mean electron−nucleus distance; κ is a dimensionless parameter accounting for the isotropic hyperfine interaction arising from admixtures with excited electronic configurations having unpaired s electron densities, both core ns orbitals (positive sign) and the valence 4s orbital (negative sign); α^2 is the fractional unpaired spin population involving the Mn orbitals and accounts for the metal−ligand covalency (58); $\xi = -^1/_{42}$ is a numerical constant depending upon the electronic configuration of the ion (77). These expressions generalize the specific case reported previously, which considered only axially symmetric ligand fields and resulted in a pure ground ^{5}A$_{1g}$ or ^{5}B$_{1g}$ state (57). The new expressions A4 are applicable

to the more general case of an orthorhombic ligand field with a mixed ground-state wave function ($\cos \delta \cdot {}^5B_1 + \sin \delta \cdot {}^5A_1$).

SUPPORTING INFORMATION AVAILABLE

Light-induced loss of the Mn^{2+} EPR signal in the pH range of 6−7.5 (Figure S1), Mn^{3+} EPR signals in the presence of varied concentrations of Mn^{2+} (Figure S2), and simulated Mn^{3+} EPR spectra at pH 6.5 and 9 (Figure S3). This material is available free of charge via the Internet at http://pubs.acs.org.

REFERENCES

1. Boussac, A., and Rutherford, A. W. (1988) The nature of the inhibition of the oxygen evolving enzyme of PSII which is induced by NaCl washing and reversed by the addition of Ca^{2+} or Sr^{2+}, *Biochemistry 27*, 3476−3483.

2. Sivaraja, M., Tso, J., and Dismukes, G. C. (1989) A calcium specific site influences the structure and activity of the manganese cluster responsible for photosynthetic water oxidation, *Biochemistry 28*, 9459−9464.

3. Kalosaka, K., Beck, W. F., Brudvig, G. W., and Cheniae, G. (1990) Coupling of the PS2 reaction center to the O_2 evolving center requires a very high affinity Ca^{2+} site, in *Research in Photosynthesis* (Baltscheffsky, M., Ed.) pp 721−724, Kluwer, Dordrecht, The Netherlands.

4. Han, K.-C., and Katoh, S. (1995) Different binding affinity sites for Ca^{2+} for reactivation of oxygen evolution in NaCl-washed photosystem II membranes represent differently modified states of a single binding site, *Biochim. Biophys. Acta 1232*, 230−236.

5. Han, K.-C., and Katoh, S. (1993) Different localization of two Ca^{2+} in spinach OEC. Evidence for involvment of only 1 Ca^{2+} in oxygen evolution, *Plant Cell Physiol. 34*, 585−593.

6. Latimer, M. J., DeRose, V. J., Mukerji, I., Yachandra, V. K., Sauer, K., and Klein, M. P. (1995) Evidence for the proximity of calcium to the manganese cluster of photosystem II: Determination by X-ray absorption spectroscopy, *Biochemistry 34*, 10898−10909.

7. Cinco, R. M., Robblee, J. H., Rompel, A., Fernandez, C., Yachandra, V. K., Sauer, K., and Klein, M. P. (1998) Strontium EXAFS reveals the proximity of calcium to the manganese cluster of OEC−PSII, *J. Phys. Chem. B 102*, 8248−8256.

8. Cinco, R. M., McFarlane Holman, K. L., Robblee, J. H., Yano, J., Pizarro, S. A., Bellacchio, E., Sauer, K., and Yachandra, V. K. (2002) Calcium EXAFS establishes the Mn−Ca cluster in the oxygen-evolving complex of photosystem II, *Biochemistry 41*, 12928−12933.

9. Sauer, K., Yano, J., and Yachandra, V. K. (2005) X-ray spectroscopy of the Mn_4Ca cluster in the water-oxidation complex of photosystem II, *Photosynth. Res. 85*, 73−86.

10. Carrell, T. G., Tyryshkin, A. M., and Dismukes, G. C. (2002) An evaluation of structural model for the photosynthetic water-oxidizing complex derived from spectroscopic and X-ray diffraction signatures, *J. Biol. Inorg. Chem. 7*, 2−22.

11. Britt, R. D., Campbell, K. A., Peloquin, J. M., Gilchrist, M. L., Aznar, C. P., Dicus, M. M., Robblee, J., and Messinger, J. (2004) Recent pulsed EPR studies of the photosystem II oxygen-evolving complex: Implications as to water oxidation mechanisms, *Biochim. Biophys. Acta Bioenerg. 1655*, 158−171.

12. Biesiadka, J., Loll, B., Kern, J., Irrgang, K. D., and Zouni, A. (2004) Crystal structure of cyanobacterial photosystem II at 3.2 Å resolution: A closer look at the Mn-cluster, *Phys. Chem. Chem. Phys. 6*, 4733−4736.

13. Ferreira, K. N., Iverson, T. M., Maghlaoui, K., Barber, J., and Iwata, S. (2004) Architecture of the photosynthetic oxygen-evolving center, *Science 303*, 1831−1838.

14. Dasgupta, J., van Willigen, R. T., and Dismukes, G. C. (2004) Consequences of structural and biophysical studies for the molecular mechanism of photosynthetic oxygen evolution: Functional roles for calcium and bicarbonate, *Phys. Chem. Chem. Phys. 6*, 4793−4802.

15. McEvoy, J. P., and Brudvig, G. W. (2004) Structure-based mechanism of photosynthetic water oxidation, *Phys. Chem. Chem. Phys. 6*, 4754−4763.

16. Messinger, J. (2004) Evaluation of different mechanistic proposals for water oxidation in photosynthesis on the basis of Mn_4O_xCa structures for the catalytic site and spectroscopic data, *Phys. Chem. Chem. Phys. 6*, 4764−4771.

17. Barber, J., Ferreira, K., Maghlaoui, K., and Iwata, S. (2004) Structural model of the oxygen-evolving centre of photosystem II with mechanistic implications, *Phys. Chem. Chem. Phys. 6*, 4737−4742.

18. Ananyev, G. M., Zaltsman, L., Vasko, C., and Dismukes, G. C. (2001) The inorganic biochemistry of photosynthetic oxygen evolution/water oxidation, *Biochim. Biophys. Acta Bioenerg. 1503*, 52−68.

19. Ono, T. (2001) Metallo-radical hypothesis for photoassembly of Mn_4-cluster of photosynthetic oxygen evolving complex, *Biochim. Biophys. Acta Bioenerg. 1503*, 40−51.

20. Tamura, N., and Cheniae, G. M. (1987) Photoactivation of the water-oxidizing complex in photosystem II membranes depleted of Mn and extrinsic proteins. I. Biochemical and kinetic characterization, *Biochim. Biophys. Acta 890*, 179−194.

21. Tamura, N., Inoue, Y., and Cheniae, G. M. (1989) Photoactivation of the water-oxidizing complex in photosystem-II membranes depleted of Mn, Ca and extrinsic proteins. 2. Studies on the functions of Ca^{2+}, *Biochim. Biophys. Acta 976*, 173−181.

22. Miller, A. F., and Brudvig, G. W. (1989) Manganese and calcium requirement for reconstitution of oxygen-evolution activity in manganese-depleted photosystem II membranes, *Biochemistry 28*, 8181−8190.

23. Zaltsman, L., Ananyev, G., Bruntrager, E., and Dismukes, G. C. (1997) A quantitative kinetic model for photo-assembly of the photosynthetic water oxidase from its inorganic constituents: Requirements for Mn and Ca in the kinetically resolved steps, *Biochemistry 36*, 8914−8922.

24. Baranov, S. V., Ananyev, G. M., Klimov, V. V., and Dismukes, G. C. (2000) Bicarbonate accelerates assembly of the inorganic core of the water-oxidizing complex in manganese-depleted photosystem II: A proposed biogeochemical role for atmospheric carbon dioxide in oxygenic photosynthesis, *Biochemistry 39*, 6060−6065.

25. Baranov, S., Tyryshkin, A., Katz, D., Dismukes, G., Ananyev, G., and Klimov, V. (2004) Bicarbonate is a native cofactor for assembly of the manganese cluster of the photosynthetic water oxidizing complex: II. Kinetics of reconstitution of O_2 evolution by photoactivation, *Biochemistry 43*, 2070−2079.

26. Dasgupta, J., Tyryshkin, A. M., Baranov, S. V., and Dismukes, G. C. Unpublished result.

27. Chen, C. G., and Cheniae, G. M. (1995) The binding of the one Ca^{2+} required in O_2-evolution is dependent on the existence of the Mn_4-cluster—Its maximum binding-affinity is almost independent of the extrinsic polypeptides, *Plant Physiol. 108*, 87.

28. Chen, C., Kazimir, J., and Cheniae, G. M. (1995) Calcium modulates the photoassembly of photosystem II (Mn_4)-clusters by preventing ligation of nonfunctional high-valency states of manganese, *Biochemistry 34*, 13511−13526.

29. Ananyev, G. M., and Dismukes, G. C. (1996) High-resolution kinetic studies of the reassembly of the tetra-manganese cluster of photosynthetic water oxidation: Proton equilibrium, cations, and electrostatics, *Biochemistry 35*, 14608−14617.

30. Yocum, C. F. (1991) Calcium activation of photosynthetic water oxidation, *Biochim. Biophys. Acta 1059*, 1−15.

31. Grove, G. N., and Brudvig, G. W. (1998) Calcium binding studies of PSII using a Ca-selective electrode, *Biochemistry 37*, 1532−1539.

32. Kelley, P. M., and Izawa, S. (1978) Role of chloride-ion in photosystem-II. 1. Effects of chloride-ion on photosystem-II electron-transport and on hydroxylamine inhibition, *Biochim. Biophys. Acta 502*, 198−210.

33. Fine, D. L., and Frasch, W. D. (1992) The oxygen evolving complex requires chloride to prevent hydrogen peroxide formation, *Biochemistry 31*, 12204−12210.

34. Lindberg, K., Vanngard, T., and Andreasson, L.-E. (1993) Studies of the slowly exchanging chloride in photosystem II of higher plants, *Photosynth. Res. 38*, 401−408.

35. Ananyev, G. M., and Dismukes, G. C. (1996) Assembly of the tetra-Mn site of photosynthetic water oxidation by photoactivation: Mn stoichiometry and detection of a new intermediate, *Biochemistry 35*, 4102−4109.

36. Carrell, T. G., Cohen, S., and Dismukes, G. C. (2002) Oxidative catalysis by $Mn_4O_4^{6+}$ cubane complexes, *J. Mol. Catal. A: Chem. 187*, 3−15.

37. Blubaugh, D. J., and Cheniae, G. M. (1992) *Photoassembly of the Photosystem II Manganese Cluster* (Murata, N., Ed.) pp 361–364, Kluwer Academic Publishers, The Netherlands.

38. Hoganson, C. W., Ghanotakis, D. F., Babcock, G. T., and Yocum, C. F. (1989) Mn^{2+} reduces Y$_z^+$ in manganese-depleted photosystem II preparations, *Photosynth. Res. 22*, 285–293.

39. Klimov, V. V., and Baranov, S. V. (2001) Bicarbonate requirement for the water-oxidizing complex of photosystem II, *Biochim. Biophys. Acta 1503*, 187–196.

40. Campbell, K. A., Force, D. A., Nixon, P. J., Dole, F., Diner, B. A., and Britt, R. D. (2000) Dual-mode EPR detects the initial intermediate in the photoassembly of the PSII Mn cluster, *J. Am. Chem. Soc. 122*, 3754–3761.

41. Berthold, D. A., Babcock, G. T., and Yocum, C. F. (1981) A highly resolved oxygen-evolving photosystem II preparation from spinach thylakoid membranes, *FEBS Lett. 27*, 231–234.

42. Ghanotakis, D. F., Babcock, G. T., and Yocum, C. F. (1984) Structural and catalytic properties of the oxygen-evolving complex—Correlation of polypeptide and manganese release with the behavior of Z$^+$ in chloroplasts and a highly resolved preparation of the PSII complex, *Biochim. Biophys. Acta 765*, 388–398.

43. Miller, A. F., and Brudvig, G. W. (1990) Electron-transfer events leading to reconstitution of oxygen-evolution activity in manganese-depleted photosystem-II membranes, *Biochemistry 29*, 1385–1392.

44. Dzuba, S. A., Watari, H., Shimoyama, Y., Maryasov, A. G., Kodera, Y., and Kawamori, A. (1995) Molecular-motion of the cholestane spin-label in a multibilayer in the gel phase studied using echo-detected EPR, *J. Mag. Reson., Ser. A 115*, 80–86.

45. Manchandra, R., Brudvig, G. W., and Crabtree, R. H. (1995) High-valent oxomanganese clusters: Structural and mechanistic work relevant to the oxygen-evolving center in photosystem II, *Coord. Chem. Rev. 144*, 1–38.

46. Khangulov, S. V., Pessiki, P. J., Barynin, V. V., Ash, D. E., and Dismukes, G. C. (1995) Determination of the metal-ion separation and energies of the 3 lowest electronic states of dimanganese-(II,II) complexes and enzymes—Catalase and liver arginase, *Biochemistry 34*, 2015–2025.

47. Hanley, J., Sarrou, J., and Petrouleas, V. (2000) Orientation of the Mn(II)–Mn(III) dimer which results from the reduction of the oxygen-evolving complex of photosystem II by NO: An electron paramagnetic resonance study, *Biochemistry 39*, 15441–15445.

48. Debus, R. J. (1992) The manganese and calcium ions of photosynthetic oxygen evolution, *Biochim. Biophys. Acta 1102*, 269–352.

49. Demeter, S., Goussias, C., Bernat, G., Kovacs, L., and Petrouleas, V. (1993) Participation of the $g = 1.9$ and $g = 1.82$ EPR forms of the semiquinone–iron complex Q$_a^-$–Fe^{2+} of photosystem-II in the generation of the Q and C thermoluminescence bands, respectively, *FEBS Lett. 336*, 352–356.

50. Kanazawa, A., Kramer, D., and Crofts, A. (1992) Temperature-dependence of PS2 electron-transfer reactions measured by flash-induced fluorescence changes, *Photosynth. Res. 34*, 139–139.

51. Golombek, A. P., and Hendrich, M. P. (2003) Quantitative analysis of dinuclear manganese(II) EPR spectra, *J. Magn. Reson. 165*, 33–48.

52. Bryliakov, K. P., Babushkin, D. E., and Talsi, E. P. (1999) Detection of EPR spectra in $S = 2$ states of Mn$_{III}$(salen) complexes, *Mendeleev Commun. 1*, 29–32.

53. Campbell, K. A., Yikilmaz, E., Grant, C. V., Gregor, W., Miller, A. F., and Britt, R. D. (1999) Parallel polarization EPR characterization of the Mn(III) center of oxidized manganese superoxide dismutase, *J. Am. Chem. Soc. 121*, 4714–4715.

54. Campbell, K. A., Lashley, M. R., Wyatt, J. K., Nantz, M. H., and Britt, R. D. (2001) Dual-mode EPR study of Mn(III) salen and the Mn(III) salen-catalyzed epoxidation of *cis-β*-methylstyrene, *J. Am. Chem. Soc. 123*, 5710–5719.

55. Maneiro, M., Bermejo, M. R., Fondo, R., Gonzalez, A. M., Sanmartin, J., Garcia-Monteagudo, J. C., Pritchard, R. G., and Tyryshkin, A. M. (2001) Structural and photolytic studies on new mononuclear and binuclear manganese complexes containing Schiff base ligands. The crystal structure of [Mn(μ-3,5-Brsalpn)-(μ-O)]$_2$2DMF, *Polyhedron 20*, 711–719.

56. Gerritsen, H. J., and Sabisky, E. S. (1963) Paramagnetic resonance of trivalent manganese in rutile (TiO$_2$), *Phys. Rev. 132*, 1507–1512.

57. Abragam, A., and Bleaney, B. (1986) *Electron Paramagnetic Resonance of Transition Ions*, Dover Publications, Inc., New York.

58. Figgis, B. N., and Hitchman, M. A. (2000) *Ligand Field Theory and Its Applications*, Wiley-VCH, New York.

59. Lever, A. B. P. (1984) *Inorganic Electronic Spectroscopy*, 2nd ed., Elsevier, Amsterdam, The Netherlands.

60. Al'tshuler, S. A., and Kozyrev, B. M. (1974) *Electron Paramagnetic Resonance in Compounds of Transition Elements*, John Wiley and Sons, New York.

61. Ghirardi, M. L., Lutton, T. W., and Seibert, M. (1996) Interactions between diphenylcarbazide, zinc, cobalt, and manganese on the oxidizing side of photosystem II, *Biochemistry 35*, 1820–1828.

62. Hsu, B.-D., Lee, J.-Y., and Pan, R.-L. (1987) The high-affinity binding site for manganese on the oxidizing side of photosystem II, *Biochim. Biophys. Acta 890*, 89–96.

63. Ananyev, G. M., Murphy, A., Abe, Y., and Dismukes, G. C. (1999) Remarkable affinity and selectivity for Cs$^+$ and uranyl (UO$_2^{2+}$) binding to the manganese site of the apo-water oxidation complex of photosystem II, *Biochemistry 38*, 7200–7209.

64. Tamura, N., and Cheniae, G. M. (1986) Requirements for the photoligation of Mn^{2+} in PSII membranes and the expression of water-oxidizing activity of the polynuclear Mn-catalyst, *FEBS Lett. 200*, 231–236.

65. Ono, T.-A., and Inoue, Y. (1983) Requirement of divalent cations for photoactivation of the latent water-oxidation system in intact chloroplasts from flashed leaves, *Biochim. Biophys. Acta 723*, 191–201.

66. Ono, T. A., and Mino, H. (1999) Unique binding site for Mn^{2+} ion responsible for reducing an oxidized Y$_Z$ tyrosine in manganese-depleted photosystem II membranes, *Biochemistry 38*, 8778–8785.

67. Klimov, V. V., Allakhverdiev, S. I., Shuvalov, V. A., and Krasnovsky, A. A. (1982) Effect of extraction and re-addition of manganese on light reactions of photosystem-II preparations, *FEBS Lett. 148*, 307–312.

68. Weltner, W. J. (1983) *Magnetic Atoms and Molecules*, Dover, New York.

69. Walker, F. A., and Sigel, H. (1972) Observation of *cis*-bis(2,2′-bipyridyl)copper(II) by electron-spin resonance, *Inorg. Chem. 11*, 1162.

70. Peisach, J., and Blumberg, W. E. (1974) Chemical composition of close-lying ligands in natural and artificial copper proteins as determined by EPR, *Fed. Proc. 33*, 1371–1371.

71. Szabo-Planka, T., Nagy, N., Rockenbauer, A., and Korecz, L. (2000) An ESR study of the copper(II)-glycyl-L-histidine system in aqueous solution by the simultaneous analysis of multi-component spectra. Formation constants and coordination modes, *Polyhedron 19*, 2049–2057.

72. Chen, C. G., and Cheniae, G. M. (1993) The photoassembly of active O$_2$-evolving Mn clusters by 17/23 kDa-less NH$_2$OH–PSII is modulated by Ca^{2+}, *Plant Physiol. 102*, 144–144.

73. Debus, R. J., Aznar, C., Campbell, K. A., Gregor, W., Diner, B. A., and Britt, R. D. (2003) Does aspartate 170 of the D1 polypeptide ligate the manganese cluster in photosystem II? An EPR and ESEEM study, *Biochemistry 42*, 10600–10608.

74. Debus, R. J. (2005) The catalytic manganese cluster: Protein ligation, in *Photosystem II: The Light Driven Water:Plastoquinone Oxidoreductase* (Wydrzynski, T., and Satoh, K., Eds.) pp 261–284, Springer, The Netherlands.

75. Ono, K., Koide, S., Sekiyama, H., and Abe, H. (1954) Paramagnetic resonance in chromous sulfate pentahydrates, *Phys. Rev. 96*, 38–39.

76. Pryce, M. H. L. (1950) Spin–spin interaction within paramagnetic ions, *Phys. Rev. 80*, 1107–1108.

77. Abragam, A., and Pryce, M. H. L. (1951) Theory of the nuclear hyperfine structure of paramagnetic resonance spectra in crystals, *Proc. R. Soc. London, Ser. A 205*, 135–153.